Journal of Computational Physics 524 (2025) 113740

Contents lists available at ScienceDirect

Journal of Computational Physics

journal homepage: www.elsevier.com/locate/jcp

Toward highly accurate multigroup coupled photon-electron-positron cross-sections for the Boltzmann Fokker-Planck equation

Charles Bienvenue [a,*], Ahmed Naceur [a], Alain Hébert [a], Jean-François Carrier [b]

[a] Institut de génie nucleaire, Polytechnique Montréal, Montréal, H3C 3A7, Canada
[b] Département de physique, Université de Montréal, Montréal, H3T 1J4, Canada

ARTICLE INFO

Keywords:
Boltzmann Fokker-Planck equation
Multigroup cross-sections
Discrete ordinates
Charged particles

ABSTRACT

For many contemporary applications, ionizing radiation transport plays a pivotal role, requiring an accurate assessment of its impact on the exposed environment. While Monte Carlo simulations are widely considered the gold standard for accurate general-purpose coupled transport of photons, electrons and positrons in matter, discrete ordinates algorithms provide a viable alternative. This work consolidates cross-section models for coupled photon-electron-positron transport and provides the methodology to generate the data required by the multigroup Boltzmann Fokker-Planck transport equation and by energy and charge deposition formulas. It includes elastic, collisional and radiative inelastic interactions of leptons, annihilation of positrons, Compton scattering, Rayleigh scattering, photoelectric effect, pair production as well as fluorescence and Auger electron production from relaxation cascades following ionization. Comparative analyses of energy deposition in water, aluminum, and gold are conducted for incident beams of 1 MeV, 10 MeV, and 100 MeV electrons and photons, and juxtaposed against Monte Carlo reference calculations. While disparities of a few percent are typical, higher deviation can be observed due to discretization or physical model limitations. Energy spectrums per particle type at varying depths in the medium are also contrasted with Monte Carlo calculations to discern limitations in the current implementation and to propose potential avenues for enhancing the presented models. Energy and charge deposition calculations are also compared to experimental measurements. The cross-section production and transport algorithms are implemented in an open-source Julia package, *Radiant.jl*.

1. Introduction

Accurate ionizing radiation transport in matter remains an outstanding challenge across various fields, including radiotherapy treatment, medical imaging, nuclear engineering, shielding, non-destructive testing, security x-ray scanning equipment, food irradiation, sterilization, and assessing radiation effects on electronics and astronauts [1,2]. Despite advancements in computational capacities in recent decades, achieving accurate estimates of quantities such as dose deposition or fluence still necessitates time-consuming calculations. This is primarily due to the complexity of all atomic interactions along particle paths with heterogeneous

* Corresponding author.
E-mail address: charles.bienvenue@polymtl.ca (C. Bienvenue).

https://doi.org/10.1016/j.jcp.2025.113740
Received 1 May 2024; Received in revised form 7 January 2025; Accepted 8 January 2025

Available online 13 January 2025

media, leading to intricate integro-differential models. Stochastic-based algorithms, also called Monte Carlo algorithms, excel in solving such complex integro-differential equations with unparalleled accuracy and are consequently considered the gold standard for energy deposition calculations [3]. Numerous general-purpose Monte Carlo codes have been developed and validated for ionizing particle transport, including GEANT4 [4,5], PENELOPE [6,7], EGSnrc [8] and MCNP6 [9]. The primary limitation of Monte Carlo solvers is their substantial demand for computational resources, notably when it is required to measure accurately low-probability events [2]. Nonetheless, it can be tricky to set some simulation parameters, such as step length with condensed Monte Carlo algorithms [10], and even if it can be significantly reduced, it is impossible to eliminate statistical noise. For these reasons, such limitations may constrain their use in many applications. For instance, radiotherapy planning requires the solution of an inverse problem, which often requires solving multiple times the direct problem, an already computationally expansive problem [11,12]. Thus, Monte Carlo methods are either set aside for clinical usage in favour of simpler, less accurate, but much faster semi-empirical models, such as pencil beams or collapsed cone convolution [13–15], or confined to limited scopes of applications by simplifying physics or geometry, implementing variance reduction techniques, or utilizing massively parallel computing architectures [16].

Yet, there are other techniques besides Monte Carlo to solve the transport equation, which is able to converge with arbitrarily high accuracy toward the exact solution [17]. Discrete ordinates solvers, a subset of the wider family of deterministic methods, have been extensively employed in nuclear engineering for neutron and photon transport [18]. However, its use for charged particle transport was not straightforward, and further development was required to ensure accurate and stable algorithms. Key advancements in this regard include the introduction of the Boltzmann Fokker-Planck approximation from Przybylski et al. [19] and the Galerkin quadrature from Morel [20,21]. Several discrete ordinates codes have been developed based on these techniques, such as the SCEPTRE code from Sandia National Laboratories [22], the ROZ-KASKAD-KATRIN codes from Keldysh Institute of Applied Mathematics [23], ACUROS from Varian Medical Systems Inc. [24], which is derived from the Attila code from Los Alamos National Laboratory [25,26], and the open-source DRAGON5 code from the Institute of Nuclear Engineering of Polytechnique Montréal [27,28]. Unlike Monte Carlo methods, these solvers do not explicitly treat random walks of individual particles. Instead, they take pre-computed multigroup cross-sections and other atomic data produced using a so-called nuclear data processing code. To this day, the coupled electron-photon cross-sections production code CEPXS from Sandia National Laboratories [29], which was released in 1989 (Version 1.0), is the only accurate multigroup production code for coupled transport of photons and electrons. Almost every work in the literature on the deterministic transport of photons and electrons is based on it, but a few exceptions where simpler models are implemented [30,31]. Currently, there is an effort to extend NJOY nuclear data code [32] capacities to electron transport through the new module ELECTR based on either on CEPXS, relying on data in restricted access, or on models using the open-source evaluated ENDF formatted data [33]. The production of pure electron cross-sections, which prohibit production of secondary particle, with CEPXS mode in ELECTR was implemented and validated over the entire periodic table up to multi-GeV energies [28,34], while the development of ENDF mode is underway [35–37]. Afterwards, coupling between the NJOY electron and photon modules, ELECTR and GAMINR, respectively, will be required in order to treat the coupled transport of these two particles similarly to CEPXS. We have noticed many drawbacks with CEPXS 1.0: 1) energy deposition cross-section calculation from CEPXS breaks down as energy discretization becomes rougher, 2) definition of the soft and catastrophic interactions leads to an ambiguous definition of stopping powers, leading to distinguishable errors, 3) CEPXS lacks the state-of-the-art models found in Monte Carlo code, such as subshell-dependent inelastic electron scattering, Rayleigh scattering or directly correlated relaxation, 4) no explicit positron cross-sections are taken into account, 5) pseudo cross-sections are produced rather than explicit stopping powers and momentum transfers and 6) its proprietary nature impedes improvements to underlying atomic interaction models, as many processes depend on hidden variables despite the CEPXS 1.0 physics guide being open access [29]. An improved CEPXS version, called CEPXS-BFP [38], proposes explicit stopping powers and momentum transfers, contrary to CEPXS 1.0, but the open access physics guide was not updated with such changes.

Hereby, we introduce RADIANT (v1.0.0), an open-source alternative to CEPXS for coupled electron-photon-positron transport, along with a discrete ordinates solver, both written in 100% pure Julia, an open-source programming language providing Python-like readability and flexibility, combined with execution times comparable to those of C++ and FORTRAN [39]. This unconventional choice was made for research purposes: by providing an open-source, easily readable, and writable code, we aim to accelerate the implementation of newer models and help the community close the gap between Monte Carlo and deterministic algorithms. We have incorporated an object-oriented framework to facilitate user interaction with the solver. The formatted cross-sections produced by RADIANT are saved in a Julia object and can be directly used by its discrete ordinates solver, but the user can choose to extract it in FMAC-M format [40] for its use with any of the aforementioned solvers. The *Radiant.jl* package can be found at [41].

In the forthcoming sections, a comprehensive overview of the algorithm is presented. First, the Boltzmann Fokker-Planck equation is introduced, serving as the foundation for the coupled particle transport. Its multigroup discretization is outlined, along with the depiction of its subtleties. Following this, the methodology for calculating energy deposition from the solution of the Boltzmann Fokker-Planck equation is specified. Subsequently, the production of macroscopic multigroup cross-sections and other atomic data for various interactions involving electrons, positrons, and photons is described. A set of benchmarks is proposed and deemed representative of the algorithm's performance for general-purpose coupled transport. Finally, the benefits of the implementation are exposed while acknowledging its current limitations and proposing potential avenues to address remaining challenges.

2. Boltzmann Fokker-Planck equation

The Boltzmann transport equation describes the transport of particles in matter, which is based on particle conservation. Widely used for decades to solve reactor physics problems [42], the direct discrete ordinates discretization of this equation was very successful, but this approach is not successful in treating particles with highly forward-peaked scattering cross-sections such as charged particles.

The Fokker-Planck (FP) equation, which is an approximate form of the transport equation assuming highly forward-peaked scattering, can be used, but it neglects important energy-loss and deviation [43]. Przybylski and Ligou proposed the Boltzmann Fokker-Planck (BFP) equation, which adds the Fokker-Planck terms to the transport equation [19]. The idea is to divide the scattering cross-sections into two domains: soft, which includes small energy-loss and angular deflection, and catastrophic, for large energy-loss and angular deflection. While the catastrophic part is treated with the Boltzmann operator, the soft part is extracted from the total and scattering cross-sections to be treated by the Fokker-Planck operator, producing soft stopping powers and momentum transfer. The two domains will be divided at an energy $E_c(E)$, which depends on the particle energy E. This relation will be defined in Sect. 2.1.

The steady-state Boltzmann Fokker-Planck equation, for a particle $p \in P = \{\gamma, \mathrm{e}-, \mathrm{e}+\}$, which correspond to photons, electrons and positrons respectively, is given by

$$\boldsymbol{\Omega} \cdot \nabla \Phi_p(\mathbf{r}, \boldsymbol{\Omega}, E) + \Sigma_t^p(\mathbf{r}, E)\Phi_p(\mathbf{r}, \boldsymbol{\Omega}, E) = Q_p^{\mathrm{FP}}(\mathbf{r}, \boldsymbol{\Omega}, E) + Q_p^{\mathrm{B}}(\mathbf{r}, \boldsymbol{\Omega}, E), \tag{1}$$

where the Fokker-Planck operator, with respectively the continuous slowing-down and angular Fokker-Planck terms, is [43]

$$Q_p^{\mathrm{FP}}(\mathbf{r}, \boldsymbol{\Omega}, E) = \frac{\partial}{\partial E}\left[S^p(\mathbf{r}, E)\Phi_p(\mathbf{r}, \boldsymbol{\Omega}, E)\right] + T^p(\mathbf{r}, E)\left[\frac{\partial}{\partial \mu}\left(1-\mu^2\right)\frac{\partial}{\partial \mu} + \frac{1}{1-\mu^2}\frac{\partial^2}{\partial \phi^2}\right]\Phi_p(\mathbf{r}, \boldsymbol{\Omega}, E) \tag{2}$$

and the Boltzmann operator, which accounts for the particle scattering and production in the medium, is [18]

$$Q_p^{\mathrm{B}}(\mathbf{r}, \boldsymbol{\Omega}, E) = \sum_{p' \in P}\int_0^\infty dE' \sum_{\ell=0}^{L}\frac{2\ell+1}{4\pi}\Sigma_{s,\ell}^{p' \to p}(\mathbf{r}, E' \to E)\sum_{m=-\ell}^{\ell} R_\ell^m(\boldsymbol{\Omega})\int_{4\pi} d^2\Omega' R_\ell^m(\boldsymbol{\Omega}')\Phi_{p'}(\mathbf{r}, \boldsymbol{\Omega}', E'), \tag{3}$$

where

- E: particle energy, in $\mathrm{m_e c^2} \approx 0.510999$ MeV (reduced electron energy), which will be used in the rest of this work for energy units;
- $\mathbf{r} = (x, y, z)$: particle position;
- $\boldsymbol{\Omega} = (\mu, \phi)$: particle direction, where μ is the direction cosine and ϕ is the azimuthal angle;
- $\Phi_p(\mathbf{r}, \boldsymbol{\Omega}, E)$: angular flux for particle p, in $\mathrm{cm}^{-2} \cdot s^{-1}$;
- $\Sigma_t^p(\mathbf{r}, E)$: macroscopic total cross-section for particle p, in cm^{-1};
- $\Sigma_{s,\ell}^{p' \to p}(\mathbf{r}, E' \to E)$: ℓ-order Legendre moment of the macroscopic scattering cross-section from energies E' to E from particle p' to particle p, in $(\mathrm{m_e c^2})^{-1} \cdot \mathrm{cm}^{-1}$;
- $S^p(\mathbf{r}, E)$: stopping power for particle p, in $\mathrm{m_e c^2} \cdot \mathrm{cm}^{-1}$;
- $T^p(\mathbf{r}, E)$: momentum transfer for particle p, in cm^{-1};
- $R_\ell^m(\boldsymbol{\Omega})$: real spherical harmonics, as defined in [18].

The energy domain is discretized, applying the Galerkin method of weighted residuals [44], in G groups, where $g = 1$ corresponds to the maximum energy group. The mean energy of the g group is defined as E_g, its width is given by ΔE_g and its upper and lower boundaries are respectively $E_{g-1/2}$ and $E_{g+1/2}$. The lower bound of the last energy group, $E_{G+1/2}$, is called the cutoff energy, under which particles are considered to be absorbed. Assuming constant flux in each energy group, for a given material, the group-averaged total cross-sections in group g of particle p are

$$\Sigma_{t,g}^p = \sum_x \left[\frac{1}{\Delta E_g}\int_{E_{g+1/2}}^{E_{g-1/2}} dE\, \Sigma_t^{p,x}(E)\right], \tag{4}$$

where the total cross-sections are given by the sum of the total cross-sections of each interaction x. The group-averaged ℓ-order Legendre moment of the scattering cross-sections from group g' of particle p' to group g of particle p are

$$\Sigma_{s,\ell,g' \to g}^{p' \to p} = \sum_x \left[\frac{1}{\Delta E_g}\int_{E_{g+1/2}}^{E_{g-1/2}} dE\, \Sigma_{s,\ell,g'}^{p' \to p,x}(E)\right] \tag{5}$$

with

$$\Sigma_{s,\ell,g'}^{p' \to p,x}(E) = \int_{E'_{g+1/2}}^{E'_{g-1/2}} dE' \int_{-1}^{1} d\mu\, P_\ell(\mu)\Sigma_s^{p' \to p,x}(E' \to E, \mu), \tag{6}$$

where $P_\ell(\mu)$ is the ℓ-order Legendre polynomial. The stopping powers at boundaries of group g for particle p, used to solve the BFP equation, are

$$S^p_{g+1/2} = \sum_x S^{p,x}(E_{g+1/2}) \quad \text{and} \quad S^p_{g-1/2} = \sum_x S^{p,x}(E_{g-1/2}), \tag{7}$$

while the group-averaged stopping powers of group g for particle p, used in the energy deposition cross-sections calculations, are

$$S^p_g = \sum_x \left[\frac{1}{\Delta E_g} \int_{E_{g+1/2}}^{E_{g-1/2}} dE\, S^{p,x}(E) \right]. \tag{8}$$

The group-averaged momentum transfers in group g for particle p, used to solve the BFP equation, are given by

$$T^p_g = \sum_x \left[\frac{1}{\Delta E_g} \int_{E_{g+1/2}}^{E_{g-1/2}} dE\, T^{p,x}(E) \right]. \tag{9}$$

While CEPXS 1.0 produce so-called pseudo cross-sections for soft interactions, which are compatible with standard S_N Boltzmann solver, RADIANT, like CEPXS-BFP, generates explicit stopping powers and momentum transfers to use with a BFP solver that explicitly discretizes the CSD and the AFP operators. There is no option, for now, to generate pseudo cross-sections like CEPXS 1.0. To solve the multigroup BFP equation, the values given by Eqs. (4)-(9) have to be calculated beforehand. The outermost integrals of these equations and every numerical quadrature mentioned in the following sections are treated using 8-point Gauss-Legendre quadrature unless noted otherwise. The values of the cross-sections, the stopping powers, and momentum transfers are given by the sum of each interaction x and are defined in the following sections. In the model, the following set of atomic interactions have been incorporated: impact ionization, elastic scattering of leptons, Bremsstrahlung production, positron annihilation, Compton scattering, photoelectric effect, pair production, Rayleigh scattering, fluorescence production and Auger electron production. Note that index x is omitted in the following section to simplify notation.

In this paper, the BFP equation is used as a generalized form of the transport equation, encompassing both the Boltzmann and FP equations. Some interactions will only be discretized for the Boltzmann transport equation, while others will use the full BFP. Therefore, the definition of the cross-sections, stopping powers, and momentum transfers can differ from the one in the Boltzmann equation or the FP equation since it depends on how each atomic interaction is discretized. For example, the Compton cross-sections are discretized for the Boltzmann equation only, while the impact ionization cross-sections are discretized for the BFP equation. Nonetheless, transport corrections are applied to the elastic cross-sections, effectively altering the values of the total and scattering cross-sections. For these reasons, the reader should refer to how the cross-sections are defined for each interaction described in the following sections. If the cross-sections, stopping powers and momentum transfers are not specified for a specific interaction, the reader should assume it equals zero.

2.1. Definition of soft and catastrophic interactions

The energy separating the soft and catastrophic domains on the energy spectrum, $E_c(E)$, is a function of E, the incident particle in a given interaction. There are two limit cases: 1) if $E_c(E) = 0$, the BFP reduces to the FP equation and 2) if $E_c(E) = E$, it reduces to the Boltzmann equation. To fully use the potential of the BFP, a choice can be made between these two limit cases. In CEPXS 1.0, the catastrophic interactions are defined as the ones in which the particle in group g down-scatter into a non-adjacent energy group, less than $E_{g+3/2}$, while with soft interactions, the particle down-scatter in the adjacent energy group [29]. This is problematic since it leads to ambiguous definitions of the soft stopping powers at group boundaries because the definition of $S^p_{g+1/2}$ differs whether it is viewed from the energy group g or $g+1$. Lorence et al. [29] address this challenge by an equal-weight averaging of these two definitions, which is somewhat arbitrary and lacks consistency with the BFP equation as presented in this paper. This method produces numerical errors in the solution of the BFP equation, which are exacerbated with rough energy discretization. For example, the relative difference between the two stopping power definitions, in each group, ranges between 3% and 25% for impact ionization in aluminum, while it ranges between 72% and 862% for bremsstrahlung, with 80 logarithmically spaced energy groups between 1 keV and 10.58 MeV, and based on the stopping powers proposed in this paper. A more robust definition can be proposed to solve such ambiguity. The definition of soft and catastrophic domains on the energy spectrum at group boundaries is shown in Fig. 1, where two points $(E, E_c(E))$ are defined as $(E_{g-1/2}, E_{g+1/2})$ and $(E_{g+1/2}, E_{g+3/2})$ for any group g, with the additional definition $E_{G+3/2} = 0$. A smooth transition between these two coordinates is required and is set to be linear in E. The resulting energy dividing the soft and catastrophic domains, for $E \in [E_{g-1/2}, E_{g+1/2}]$, is given by

$$E_c(E) = \left(\frac{E_{g+1/2} - E_{g+3/2}}{E_{g-1/2} - E_{g+1/2}} \right) E - \frac{E^2_{g+1/2} - E_{g-1/2} E_{g+3/2}}{E_{g-1/2} - E_{g+1/2}} \tag{10}$$

for any $1 \le g \le G$. This new definition solves the ambiguity of the definition of soft stopping powers, cancelling out the numerical issues it could generate.

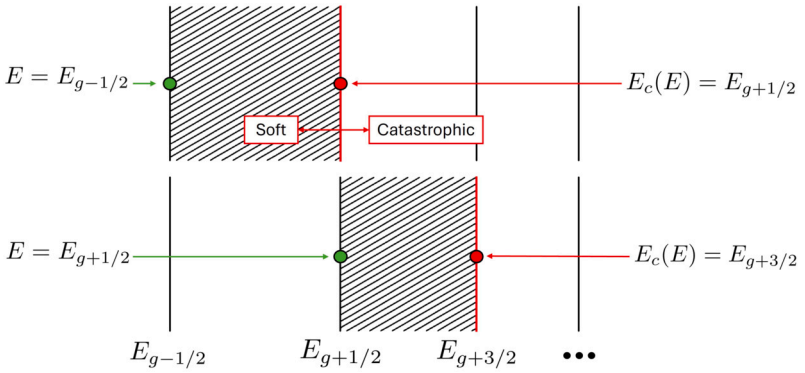

Fig. 1. Definition of the soft and catastrophic interactions at energy group boundaries. The green dots represent the energy of the incident particle interacting with the medium, while the red dots correspond to the cutoff energies between soft and catastrophic energy domains. The cutoff energy corresponding to any incident particle energy anywhere in the group g, or between $E_{g-1/2}$ and $E_{g+1/2}$, is given by Eq. (10). (For interpretation of the colours in the figure(s), the reader is referred to the web version of this article.)

2.2. Energy deposition

The solution of the BFP for each particle p, in each voxel j of volume V_j and in each energy group g is given by the integrated flux $\Phi^p_{g,j}$. Such integrated flux can be used to compute reaction rates such as energy deposition or charge deposition. The volume V_j is given in $\mathrm{cm}^{N_{\mathtt{dim}}}$, with $N_{\mathtt{dim}}$ is the geometry dimension. The total energy deposition in voxel j, in $\mathrm{m_e c^2/g \times cm^{3-N_{dim}}}$, is given by [29,45]

$$D_j = \frac{1}{\rho V_j} \sum_{p\in P} \left\{ \sum_{g=1}^{G} \Sigma^p_{e,g,j} \Phi^p_{g,j} + \Sigma^p_{e,G+1,j} \Phi^p_{G+1/2,j} \right\} \quad \text{with} \quad \Sigma^p_{e,g,j} = \sum_x \Sigma^{p,x}_{e,g,j}\,, \tag{11}$$

where ρ is the medium density in $\mathrm{g/cm^3}$. $\Phi^p_{G+1/2,j}$ is the flux evaluated at the cutoff energy $E_{G+1/2}$. The first term of the total energy deposition formula corresponds to the net energy deposited in each energy group, while the second term is required with the BFP equation, due to the CSD operator, to take into account particle slowing-down to the energy cutoff [45]. The energy deposition cross-sections, $\Sigma^p_{e,g,j}$, is the sum of the $\Sigma^{p,x}_{e,g,j}$ for each interaction x in energy group g for incident particle p. The energy deposition cross-sections for a given interaction x, which characterize the net energy gain or loss following that interaction, are given by

$$\Sigma^{p,x}_{e,g} = S^{p,x}_g + \frac{1}{\Delta E_g} \int_{E_{g+1/2}}^{E_{g-1/2}} dE \left\{ (E - \Delta Q_x)\Sigma^{p,x}_t(E) - \sum_{p'\in P} \left[\int_{E_{G+1/2}}^{E} dE'\, E' \Sigma^{p\to p',x}_{s,0}(E \to E') \right] - \Sigma^{p,x}_{\mathrm{uc}}(E) \right\}, \tag{12}$$

for $1 \le g \le G$. It encompasses the CSD energy-loss in the group, the kinetic energy of the interaction's incident particle in the group, the kinetic energy of the particle leaving the interaction, and the variation of rest mass energy of the nucleus and the elementary particle, given by ΔQ_x ($\Delta Q_x > 0$ for increase in mass, $\Delta Q_x < 0$, for a decrease in mass) [46]. For example, the pair production interaction causes an electron and a positron to appear, which correspond to $\Delta Q_x = 2\ \mathrm{m_e c^2}$. Conversely, the annihilation interaction makes the incoming positron and an atomic electron disappear, resulting in a decrease of mass of $\Delta Q_x = -2\ \mathrm{m_e c^2}$. No mass change occurs in interaction such as Compton or elastic scattering, i.e. $\Delta Q_x = 0$. The last term, $\Sigma^{p,x}_{\mathrm{uc}}(E)$, corresponds to the particle production from processes occurring under the cutoff energy, which is restricted to positron annihilation in this work. Physically, positrons always end up annihilating by producing two photons. Three interactions x' can scatter or produce positrons under the energy cutoff $E_{G+1/2}$, following either 1) catastrophic impact ionization positron interactions, 2) catastrophic positron-induced Bremsstrahlung interactions, or 3) following pair production. To take the annihilation of these positrons, which scatter under the cutoff, into account, the following contribution,

$$\Sigma^{p,x}_{\mathrm{uc}}(E) = \int_0^{E_{G+1/2}} dE' (\Delta Q' + \Delta Q_x + E') \Sigma^{p\to p',x'}_{s,0}(E \to E')\,, \tag{13}$$

should be added to the energy deposition, with $p' = \gamma$ and $\Delta Q' = -2\ \mathrm{m_e c^2}$, corresponding respectively to the annihilation photon and the loss of rest mass energy in annihilation. The annihilation cross-sections under the cutoff energy are given in Sect. 6.4. There is another contribution to energy deposition with the BFP equation due to soft interaction, which causes particles to slow down until they reach the cutoff, where they are absorbed locally. The energy deposition cross-sections at the cutoff energy are given by [1,45]

$$\Sigma^{p,x}_{e,G+1} = E_{G+1/2} \frac{S^p_{G+1/2,j}}{\Delta E_G}\,, \tag{14}$$

where $S^p_{G+1/2,j}$ is the soft stopping power at the cutoff energy.

2.3. Charge deposition

The total charge deposition in voxel j, in $\mathrm{cm}^{3-N_{\mathtt{dim}}}/\mathrm{g}$, is given by [1,29]

$$C_j = \frac{1}{\rho V_j} \sum_{p\in P} \left\{ \sum_{g=1}^{G} \Sigma^p_{c,g,j} \Phi^p_{g,j} + \Sigma^p_{c,G+1,j} \Phi^p_{G+1/2,j} \right\} \quad \text{with} \quad \Sigma^p_{c,g,j} = \sum_x \Sigma^{p,x}_{c,g,j}\,, \tag{15}$$

where the charge deposition cross-sections for a given interaction x are given by

$$\Sigma^{p,x}_{c,g} = -\frac{1}{\Delta E_g} \int_{E_{g+1/2}}^{E_{g-1/2}} dE \left\{ q_p \Sigma^{p,x}_t(E) - \sum_{p'\in P} \delta_x q_{p'} \left[\int_{E_{G+1/2}}^{E} dE'\, \Sigma^{p\to p',x}_{s,0}(E\to E') \right] \right\} \tag{16}$$

for $1 \le g \le G$, where q_p is the particle charge given by

$$q_p = \begin{cases} -1 & \text{if } p = \mathtt{e}\text{-} \\ 0 & \text{if } p = \gamma \\ 1 & \text{if } p = \mathtt{e}\text{+} \end{cases} \tag{17}$$

and where δ_x is a parameter to account for particles that are neither extracted from the medium nor deposited in it. For pair production, it is given by $\delta_x = 0$ since the electron-positron pair does not change the net charge of the medium. Otherwise, $\delta_x = 1$. As for dose deposition, there is a charge deposition component at the cutoff energy due to soft interaction. The charge deposition cross-sections at the cutoff energy are given by [1]

$$\Sigma^{p,x}_{c,G+1} = -q_p \frac{S^p_{G+1/2,j}}{\Delta E_G}\,. \tag{18}$$

3. Impact ionization for electrons and positrons

3.1. Catastrophic impact ionization cross-section

The total impact ionization cross-section describes the interaction of an incoming electron ($p' = \mathtt{e}\text{-}$) or positron ($p' = \mathtt{e}\text{+}$) with an atomic electron. Such interaction results in the scattering of the incoming particle ($p' = \mathtt{e}\text{-}$ or $p' = \mathtt{e}\text{+}$) and the production of knock-on electrons ($p' = \mathtt{e}\text{-}$). Since catastrophic collisions don't deal with small energy loss, distant collisions are neglected in the catastrophic cross-section model. The collisional inelastic differential cross-section in the energy of the knock-on electron in a monoelemental material i is given by the sum of the differential cross-section per electron subshell k [7,29,47]

$$\sigma^i_s(E\to W) = \sum_{k=1}^{N_{\mathtt{shells}}} Z_{i,k}\, \sigma^{i,k}_s(E\to W)\,, \tag{19}$$

where $Z_{i,k}$ is the mean number of electrons in subshells k for element i, E is the incoming electron or positron energy, E' is the scattered electron or positron energy and $W = E - U_{i,k} - E'$ is the knock-on electron energy, where $U_{i,k}$ is the binding energy of the k^{th} subshell. The values of $Z_{i,k}$ and $U_{i,k}$ are extracted from Perkins et al. [48]. The close interaction cross-section is given by

$$\sigma^{i,k}_s(E\to W) = \frac{2\pi r_e^2}{\beta^2} F^{\pm}_{i,k}(E,W)\,, \tag{20}$$

where $r_e \approx 2.81794 \times 10^{-13}$ cm is the classical electron radius, the Møller factor, for electrons, is given by [49,50]

$$F^-_{i,k}(E,W) = \frac{1}{(W+U_{i,k})^2} + \frac{1}{(E-W)^2} + \frac{1}{(E+1)^2} - \frac{(2E+1)}{(E+1)^2(E-W)(W+U_{i,k})} \tag{21}$$

and the Bhabha factor, for positrons, is given by [51]

$$F^+_{i,k}(E,W) = \frac{1}{(W+U_{i,k})^2} \left[1 - b_1 \left(\frac{W+U_{i,k}}{E}\right) + b_2 \left(\frac{W+U_{i,k}}{E}\right)^2 - b_3 \left(\frac{W+U_{i,k}}{E}\right)^3 + b_4 \left(\frac{W+U_{i,k}}{E}\right)^4 \right], \tag{22}$$

where

$$b_1 = \left(\frac{\gamma-1}{\gamma}\right)^2 \frac{2(\gamma+1)^2-1}{\gamma^2-1}\,,\; b_2 = \left(\frac{\gamma-1}{\gamma}\right)^2 \frac{3(\gamma+1)^2+1}{(\gamma+1)^2}\,,$$
$$b_3 = \left(\frac{\gamma-1}{\gamma}\right)^2 \frac{2\gamma(\gamma-1)}{(\gamma+1)^2}\,,\; b_4 = \left(\frac{\gamma-1}{\gamma}\right)^2 \frac{(\gamma-1)^2}{(\gamma+1)^2}\,, \tag{23}$$

with respectively the ratio of the particle velocity to the speed of light and the Lorentz factor given by

$$\beta^2 = \frac{E(E+2)}{(E+1)^2} \quad \text{and} \quad \gamma = E+1\,. \tag{24}$$

The scattering angles for the incoming particle and knock-on electron are respectively [29]

$$\mu_p = \sqrt{\frac{E'(E+2)}{E(E'+2)}} \quad \text{and} \quad \mu_s = \sqrt{\frac{W(E+2)}{E(W+2)}}\,, \tag{25}$$

and their double differential cross-sections are respectively given by

$$\sigma_s(E\to E',\mu) = \frac{1}{2\pi}\sigma_s(E\to E')\delta(\mu-\mu_p) \quad \text{and} \quad \sigma_s(E\to W,\mu) = \frac{1}{2\pi}\sigma_s(E\to W)\delta(\mu-\mu_s)\,. \tag{26}$$

The maximum energy of knock-on for incoming electron and positron, which results from classical kinematics and the indistinguishability of electrons, is given respectively by

$$W^-_{\mathtt{max}} = \frac{E-U_{i,k}}{2} \quad \text{and} \quad W^+_{\mathtt{max}} = E-U_{i,k}\,. \tag{27}$$

3.1.1. Scattering cross-sections for incoming electrons or positrons

The Legendre moments of the differential scattering cross-sections are given by

$$\sigma^{i,k}_{s,\ell}(E\to E') = 2\pi\int_{-1}^{1} d\mu\, P_\ell(\mu)\sigma^{i,k}_s(E\to E',\mu) = P_\ell(\mu_p)\sigma^{i,k}_s(E\to E')\,. \tag{28}$$

The macroscopic Legendre moments of the scattering cross-sections for particle scattering from group g' are therefore given by

$$\Sigma^{\mathtt{e}\pm\to\mathtt{e}\pm}_{s,\ell,g'}(E) = \sum_{i=1}^{N_e}\mathcal{N}_{n,i}f_i\sum_{k=1}^{N_{\mathtt{shells}}}Z_{i,k}\int_{\max\left\{E'_{g+1/2},W^\pm_{\mathtt{max}}\right\}}^{\min\left\{E'_{g-1/2},E_c(E),E-U_{i,k}\right\}} dE'\sigma^{i,k}_{s,\ell}(E\to E')\mathcal{H}_b\,, \tag{29}$$

where the density of the i^{th}-element in the medium is given by

$$\mathcal{N}_{n,i} = \frac{\rho N_a}{A_i}\,, \tag{30}$$

with A_i is the atomic weight of the i^{th}-element, N_a is the Avogadro constant, ρ is the medium density, f_i is the weight fraction of the i^{th}-element of the compound, N_e is the number of elements in the compound and $\mathcal{H}_b$ is a Heaviside function on the difference between upper and lower integral bounds and will often be used to this end in the rest of this paper. This equation is solved using numerical quadrature.

3.1.2. Scattering cross-sections for knock-on electrons

The Legendre moments of the differential scattering cross-sections are given by

$$\sigma^{i,k}_{s,\ell}(E\to W) = 2\pi\int_{-1}^{1} d\mu\, P_\ell(\mu)\sigma^{i,k}_s(E\to W,\mu) = P_\ell(\mu_s)\sigma^{i,k}_s(E\to W)\,. \tag{31}$$

The multigroup Legendre moments of the scattering cross-sections are therefore given by

$$\Sigma^{\mathtt{e}\pm\to\mathtt{e}^-}_{s,\ell,g'}(E) = \sum_{i=1}^{N_e}\mathcal{N}_{n,i}f_i\sum_{k=1}^{N_{\mathtt{shells}}}Z_{i,k}\int_{E'_{g+1/2}}^{\min\left\{E'_{g-1/2},W^\pm_{\mathtt{max}}\right\}} dW\sigma^{i,k}_{s,\ell}(E\to W)\mathcal{H}_b\,. \tag{32}$$

This equation is solved using numerical quadrature.

3.1.3. Catastrophic total cross-sections

The catastrophic impact ionization total cross-sections are defined by

$$\Sigma_t^{e\pm}(E) = \sum_{i=1}^{N_e} \mathcal{N}_{n,i} f_i \sum_{k=1}^{N_{\text{shells}}} Z_{i,k} \int_{E-E_c(E)}^{W_{\max}^{\pm}} dW \sigma_{s,0}^{i,k}(E \to W) \mathcal{H}_b \,, \tag{33}$$

which is solved analytically.

3.1.4. Absorption cross-sections for incoming positrons

The absorption cross-sections for impact ionization interaction with incoming positrons, which include only catastrophic contributions and are required for annihilation calculations, are given by

$$\Sigma_a^{\text{inel}}(E) = \sum_{i=1}^{N_e} \mathcal{N}_{n,i} f_i \sum_{k=1}^{N_{\text{shells}}} Z_{i,k} \int_{E-\min\{E_{G+1/2}, E_c\}}^{E} dW \sigma_{s,0}^{i,k}(E \to W) \mathcal{H}_b \,, \tag{34}$$

which is solved analytically. The inclusion of annihilation photon due to absorption of positrons following soft interaction will require improved impact ionization models that are accurate for low energy loss interactions.

3.2. Total stopping power

The total collisional stopping powers of electron and positron for any compound, in $m_e c^2 \times \text{cm}^{-1}$, are given by the density- and shell-corrected Bethe formula [52]

$$S_t(E) = \frac{2\pi r_e^2}{\beta^2} \mathcal{N}_e^{\text{eff}} \left[\ln\left\{ \frac{E+2}{2} \left(\frac{E}{I^{\text{eff}}} \right)^2 \right\} + f^{(\pm)} - \delta_F - 2C(E) \right] , \tag{35}$$

where E is the energy of the incoming electron or positron, $\mathcal{N}_e^{\text{eff}}$ is the effective electron density in the medium given by

$$\mathcal{N}_e^{\text{eff}} = \sum_{i=1}^{N_e} \mathcal{N}_{n,i} f_i Z_i \,, \tag{36}$$

with f_i is the weight percent of the i^{th}-element of the compound, Z_i is the atomic number of the i^{th}-element of the compound. We also have δ_F, which is the Fermi density effect, defined in the next subsection, $C(E)$ is the shell correction, extracted from SBETHE program files [52], a state-of-the-art program to compute stopping power of charged particle, and I^{eff} is the effective mean excitation energy of the compound is given by [7]

$$I^{\text{eff}} = \exp\left\{ \frac{1}{Z^{\text{eff}}} \sum_{i=1}^{N_e} f_i Z_i \log(I_i) \right\} \quad \text{with} \quad Z^{\text{eff}} = \sum_{i=1}^{N_e} f_i Z_i \,, \tag{37}$$

where the mean excitation energy of the i^{th}-element of the compound is I_i (tabulated by Seltzer and Berger [53]), unless more accurate value is provided. For water, $I^{\text{eff}} = 78$ eV is used, as recommended by the ICRU report 90 [54,55]. The electron factor $f^{(-)}$ is given by [56]

$$f^{(-)} = 1 - \beta^2 - \frac{(2E+1)}{(E+1)^2} \ln(2) + \frac{1}{8} \left(\frac{E}{E+1} \right)^2 \tag{38}$$

and the positron factor $f^{(+)}$ is given by

$$f^{(+)} = 2\ln(2) - \frac{\beta^2}{12} \left[23 + \frac{14}{E+2} + \frac{10}{(E+2)^2} + \frac{4}{(E+2)^3} \right] . \tag{39}$$

3.2.1. Fermi density effect

The following calculation of the Fermi density effect is the same as described in SBETHE and the same used in the Monte Carlo transport code PENELOPE [7]. It is based on the formula from Fano [57,58], which is

$$\delta_F = \frac{1}{Z^{\text{eff}}} \sum_{i=1}^{N_e} \sum_{k=1}^{N_{\text{shells}}} f_i Z_{i,k} \ln\left(1 + \frac{L^2}{W_{i,k}^2} \right) - \frac{L^2}{\Omega_p^2} (1 - \beta^2) \,, \tag{40}$$

where L is given by solving

$$(1 - \beta^2) = \frac{\Omega_p^2}{Z^{\text{eff}}} \sum_{i=1}^{N_e} \sum_{k=1}^{N_{\text{shells}}} \frac{f_i Z_{i,k}}{W_{i,k}^2 + L^2} \,. \tag{41}$$

The plasma energy is given by

$$\Omega_p^2 = 4\pi \mathcal{N}_e^{\texttt{eff}} \hbar^2 c^2 r_e^2 \tag{42}$$

and the resonance energy in the $i^{\texttt{th}}$-subshell is [59]

$$W_{i,k} = \sqrt{(aU_{i,k})^2 + \frac{2}{3}\frac{Z_{i,k}}{Z_i}\Omega_p^2}, \tag{43}$$

where a is given by solving

$$Z_i \ln\left(I^{\texttt{eff}}\right) = \sum_{k=1}^{N_{\texttt{shells}}} Z_{i,k} \ln\left(\sqrt{(aU_{i,k})^2 + \frac{2}{3}\frac{Z_{i,k}}{Z_i}\Omega_p^2}\right). \tag{44}$$

3.2.2. Soft stopping powers

The inelastic collisional soft stopping power, $S^{\texttt{e}\pm}(E)$, is given by removing the catastrophic stopping power from the total stopping power. It is given by

$$S^{\texttt{e}\pm}(E) = S_t(E) - \sum_{i=1}^{N_e} \mathcal{N}_{n,i} f_i \sum_{k=1}^{N_{\texttt{shells}}} Z_{i,k} \int_{E-E_c(E)}^{W_{\texttt{max}}^{\pm}} dW (W + U_{i,k}) \sigma_{s,0}^{i,k}(E \to W) \mathcal{H}_b, \tag{45}$$

which is solved analytically.

4. Elastic scattering for electrons and positrons

The Mott cross-section describes the elastic interaction of an incoming electron ($p = p' = \texttt{e-}$) or positron ($p = p' = \texttt{e+}$) with the Coulomb field of an atom. The microscopic differential scattering cross-section in a monoelemental material i is given by

$$\sigma_s^i(E,\mu) = \frac{2\pi Z_i (Z_i + \xi_i^{\pm}) r_e^2}{\beta^2 E(E+2)} \frac{1}{(1-\mu+2\eta_i)^2} \mathcal{R}_{\texttt{Mott}}^i, \tag{46}$$

with η, the Molière screening factor with Seltzer's adjustment factor, given by [60,61]

$$\eta_i = \frac{\alpha^2 Z_i^{2/3}\left(1.13 + 3.76\left(\frac{Z_i\alpha}{\beta}\right)^2 \sqrt{\frac{E}{E+1}}\right)}{4\left(\frac{9\pi^2}{128}\right)^{2/3} E(E+2)}, \tag{47}$$

where $\alpha \approx 1/137$ is the fine structure constant. The Seltzer's adjustment factor extends the validity of the Mott cross-sections to lower energies [60]. Note that when the incoming electron or positron has increasingly more kinetic energy, η becomes very small, and the scattering cross-section becomes increasingly large as μ tends to 1, producing highly forward-peaked scattering. Lijian et al. [62] proposed the following interpolation formula for $\mathcal{R}_{\texttt{Mott}}^i$, the ratio of the unscreened Mott differential cross-section to Rutherford's cross-section:

$$\mathcal{R}_{\texttt{Mott}}^i = \sum_{j=0}^{4} a_{i,j}(1-\mu)^{j/2}, \quad \text{where} \quad a_{i,j} = \sum_{k=1}^{6} b_{k,j}(Z_i)\left(\beta - \bar{\beta}\right)^{k-1} \tag{48}$$

and $\bar{\beta} = 0.7181287$. Boschini et al. [63] have generated $b_{k,j}(Z_i)$ parameters for any $Z_i \leq 118$, for both electron and positron, and these are valid for energies between 1 keV and 900 MeV.

For incoming electrons or positrons, to take into account atomic electron contribution to the multiple scattering of charged particle transport, Z^2 is often replaced by $Z(Z+1)$ [64]. However, a double counting issue was observed in Monte Carlo codes due to an overlap with knock-on electrons [65], which are already taken into account by the Møller and Bhabha models (see Sect. 3.1). Kawrakow proposed a correction for this issue, which is significant for low Z material or when cutoff energy $E_{G+1/2}$ is low [66]. This correction is given by

$$\xi_i^{\pm} = 1 - \frac{g_{\texttt{inel},i}^{\pm}}{g_{\texttt{el},i}}, \tag{49}$$

with $g_{\texttt{el},i}$, which is calculated using the methodology described by Kawrakow for the Mott cross-sections rather than the screened Rutherford ones, is given by

$$g_{\texttt{el},i} = \frac{\tilde{\sigma}_{s,0}^i(E) - \tilde{\sigma}_{s,2}^i(E)}{3}, \tag{50}$$

where $\tilde{\sigma}^{i}_{s,\ell}(E)$ is given by Eq. (53), and with $g_{\texttt{inel},i}$ is given by

$$g^{\pm}_{\texttt{inel},i} = \sum_{k=1}^{N_{\texttt{shells}}} \frac{Z_{i,k}}{Z_i} E(E+2) \int_{E_{G+1/2}}^{W^{\pm}_{\texttt{max}}} dW \left(1-\mu_p^2\right) F^{\pm}_{i,k}(E,W)\mathcal{H}_b\,, \tag{51}$$

where $E_{G+1/2}$ is the minimum energy transfer to knock-on electron, $W^{\pm}_{\texttt{max}}$ is given by Eq. (27), μ_p, by Eq. (25) and $F^{\pm}_{i,k}(E,W)$, by Eq. (21)-(22).

4.1. Legendre moments of the scattering cross-sections

For deterministic transport calculations, the Legendre moments of the elastic cross-sections are required, namely

$$\Sigma^{\texttt{e}\pm\rightarrow\texttt{e}\pm}_{s,\ell}(E) = \sum_{i=1}^{N_e} \mathcal{N}_{n,i} f_i \int_{-1}^{1} d\mu P_\ell(\mu)\sigma^{i}_{s}(E,\mu) = \sum_{i=1}^{N_e} \mathcal{N}_{n,i} f_i \frac{2\pi Z_i(Z_i+\xi^{\pm}_i)r_e^2}{\beta^2 E(E+2)} \tilde{\sigma}^{i}_{s,\ell}(E) \tag{52}$$

with the following definition

$$\tilde{\sigma}^{i}_{s,\ell}(E) = \int_{-1}^{1} d\mu P_\ell(\mu) \frac{\mathcal{R}^{i}_{\texttt{Mott}}}{(1-\mu+2\eta_i)^2}\,. \tag{53}$$

Calculating these Legendre moments using numerical quadrature is highly inefficient due to the near singularity that often occurs at $\mu = 1$ when η is small. As demonstrated in the following lines, the integration can be fast, done analytically and in a way that ensures numerical stability.

First, the Legendre polynomial can be expressed as a sum of powers of μ as [67]

$$P_\ell(\mu) = \frac{1}{2^\ell} \sum_{k=0}^{\lfloor \ell/2 \rfloor} C_{\ell,k}\mu^{\ell-2k}\,, \quad \text{where} \quad C_{\ell,k} = \frac{(-1)^k(2\ell-2k)!}{k!(\ell-k)!(\ell-2k)!} \tag{54}$$

and therefore, the Legendre moments can be expressed as

$$\tilde{\sigma}^{i}_{s,\ell}(E) = \frac{1}{2^\ell} \sum_{k=0}^{\lfloor \ell/2 \rfloor} C_{\ell,k} \int_{-1}^{1} d\mu \frac{\mathcal{R}^{i}_{\texttt{Mott}}}{(1-\mu+2\eta_i)^2} \mu^{\ell-2k} = \frac{1}{2^\ell} \sum_{k=0}^{\lfloor \ell/2 \rfloor} C_{\ell,k} \sum_{j=1}^{2} I_j^{\ell,k}\,, \tag{55}$$

where $I_1^{\ell,k}$ is given by

$$\begin{aligned} I_1^{\ell,k} &= \int_{-1}^{1} d\mu \frac{\mu^{\ell-2k}}{(1-\mu+2\eta_i)^2} \left[\alpha_{i,0} + \alpha_{i,1}\mu + \alpha_{i,2}\mu^2\right] \\ &= \sum_{j=0}^{2} \alpha_{i,j} \left(\mathcal{G}_1^{\ell-2k+j}(1+2\eta_i,-1,1) - \mathcal{G}_1^{\ell-2k+j}(1+2\eta_i,-1,-1)\right) \end{aligned} \tag{56}$$

and $I_2^{\ell,k}$ is given by

$$\begin{aligned} I_2^{\ell,k} &= \int_{-1}^{1} d\mu \frac{\mu^{\ell-2k}\sqrt{(1-\mu)}}{(1-\mu+2\eta)^2} \left[\alpha_3 + \alpha_4\mu\right] \\ &= 2\sum_{j=0}^{2} \alpha_{i,j+3} \sum_{g=0}^{\ell-2k+j} (-1)^g \frac{(\ell-2k+j)!}{g!(\ell-2k+j-g)!} \mathcal{G}_2^{2+2g}(2\eta_i,1,\sqrt{2})\,, \end{aligned} \tag{57}$$

with $\alpha_{i,0} = a_{i,0} + a_{i,2} + a_{i,4}$, $\alpha_{i,1} = -(a_{i,2} + 2a_{i,4})$, $\alpha_{i,2} = a_{i,4}$, $\alpha_{i,3} = a_{i,1} + a_{i,3}$ and $\alpha_{i,4} = -a_{i,3}$. The first integral is solved using the following integral from Gradshteyn et al. (Eq. 4, Sect. 2.111) [68]

$$\mathcal{G}_1^n(a,b,x) = \sum_{g=1}^{n-1} (-1)^{g-1} \frac{g a^{g-1} x^{n-g}}{(n-g)b^{g+1}} + (-1)^{n-1} \frac{a^n}{b^{n+1}(a+bx)} + (-1)^{n+1} \frac{n a^{n-1}}{b^{n+1}} \ln(a+bx)\,, \tag{58}$$

while the second integral is solved by applying the change of variable $u = \sqrt{1-\mu}$, using the binomial theorem and then formulae from Gradshteyn et al. (Sect. 2.172, Eq. 1 Sect. 2.173 and Eq. 1 Sect. 2.174)

$$\mathcal{G}_2^n(a,b,x) = \begin{cases} \dfrac{x}{2aR} + \dfrac{1}{2a\sqrt{ab}} \arctan\left(\dfrac{bx}{\sqrt{ab}}\right) & n = 0 \\ -\dfrac{x^{n-1}}{(3-n)bR} + \dfrac{(n-1)a}{(3-n)b}\mathcal{G}_2^{n-2}(a,b,x) & n \text{ even} > 0 \end{cases} . \tag{59}$$

This fully analytical solution can be numerically unstable because of catastrophic cancellations for high-order Legendre terms when η is large (> 1), which happens when the elastic scattering becomes more or less isotropic, notably at low energies. Since an isotropic flux is characterized by $\ell \geq 1$ Legendre moments equal to zero, the following correction for $\ell_x \geq 1$ is proposed:

$$\textbf{if} \quad \left|\sigma^i_{s,\ell_x}(E)\right| > \left|\sigma^i_{s,0}(E)\right| \quad \textbf{then} \quad \sigma^i_{s,\ell}(E) = 0 \quad \forall\, \ell \geq \ell_x\,, \tag{60}$$

which are based on the upper bound of the high-order Legendre polynomial [69].

4.2. Total cross-sections

The elastic total cross-sections are given by

$$\Sigma_t^{e\pm}(E) = \Sigma_{s,0}^{e\pm\to e\pm}(E)\,. \tag{61}$$

4.3. Transport correction and elastic decomposition in soft and catastrophic components

The elastic scattering cross-sections can be decomposed into soft and catastrophic components [70]. Let L be the order of the cross-sections Legendre expansion and $\Sigma_{s,\ell,g\to g}^{e\pm\to e\pm}$ be the ℓ-order Legendre moment of the elastic scattering cross-section in group g. Let $L_{\max} \leq L$ be the last non-zero Legendre moments of the scattering in group g. The Legendre moments of the soft are assumed to be given by

$$\Sigma_{s,\ell,g\to g}^{e\pm\to e\pm,\mathtt{soft}} = \Sigma_{s,0,g\to g}^{e\pm\to e\pm,\mathtt{soft}} - T_g\ell(\ell+1) \tag{62}$$

for $\ell \in \{1, ..., L_{\max}\}$. This expression is obtained by establishing equality between the eigenvalues of the Boltzmann, and the AFP operator applied to the Legendre polynomials [71]. This method sets a relation, which depends on two undefined parameters $\Sigma_{s,0,g\to g}^{e\pm\to e\pm,\mathtt{soft}}$ and T_g, such as moments of the Boltzmann operator is preserved by the Fokker-Planck operator. Landesman and Morel [70] proposed to equate $\Sigma_{s,L_{\max}-1}^{e\pm\to e\pm,\mathtt{soft}} = \Sigma_{s,L_{\max}-1,g\to g}^{e\pm\to e\pm}$ and $\Sigma_{s,L_{\max},g\to g}^{e\pm\to e\pm,\mathtt{soft}} = \Sigma_{s,L_{\max},g\to g}^{e\pm\to e\pm}$ to define these parameters, which results in

$$T_g = \frac{\Sigma_{s,L_{\max}-1,g\to g}^{e\pm\to e\pm} - \Sigma_{s,L_{\max},g\to g}^{e\pm\to e\pm}}{2L_{\max}}\,, \tag{63}$$

and

$$\Sigma_{s,0,g\to g}^{e\pm\to e\pm,\mathtt{soft}} = \Sigma_{s,L_{\max},g\to g}^{e\pm\to e\pm} + T_g L_{\max}(L_{\max}+1)\,. \tag{64}$$

The soft component of the elastic cross-sections should then be withdrawn from cross-sections since the AFP operator, jointly with the momentum transfer given by Eq. (63), is used to treat that soft scattering. The total elastic cross-sections, used in transport calculations, are redefined as

$$\tilde{\Sigma}_{t,g} = \Sigma_{t,g} - \Sigma_{s,L_{\max},g\to g}^{e\pm\to e\pm} - T_g L_{\max}(L_{\max}+1)\,, \tag{65}$$

and the ℓ-order Legendre moment of the scattering cross-sections is redefined as

$$\tilde{\Sigma}_{s,\ell,g\to g}^{e\pm\to e\pm} = \Sigma_{s,\ell,g\to g}^{e\pm\to e\pm} - \Sigma_{s,L_{\max},g\to g}^{e\pm\to e\pm} - T_g\left[L_{\max}(L_{\max}+1) - \ell(\ell+1)\right]\,. \tag{66}$$

The goal of this operation is to transfer the handling of forward-peaked scattering from the Boltzmann operator, which encounters monotonicity issues with such scattering [72], to the Fokker-Planck operator, which can be tackled by finite-difference discretization schemes [73,74].

This method, as presented, also includes the extended transport correction [75,76]. The transport correction is a crucial technique that reduces the amplitude of elastic cross-sections for the BFP solver while preserving the flux solution, given that the Galerkin quadrature method is employed. [72]. This amplitude reduction aims to reduce the scattering ratio, which is very close to one in charged particle transport. Without this correction, the source iteration process would require many orders of magnitude more iterations, thus requiring a long time to converge [20].

5. Bremsstrahlung

The bremsstrahlung cross-section describes the interaction of an incoming electron ($p' = \mathtt{e}\text{-}$) or positron ($p' = \mathtt{e}\text{+}$) with the field of the atomic nucleus and its electrons. The incoming particle scatter ($p = \mathtt{e}\text{-}$ or $p = \mathtt{e}\text{+}$), while a photon is produced ($p = \gamma$). Seltzer and

Berger proposed tables to compute the differential cross-section as a function of the energy of the produced photon, which includes both electron-nucleus and electron-electron interactions, and for monoelemental material i, it is given by [77]

$$\sigma_s^i(E \to E_\gamma) = \begin{cases} \dfrac{F_{p,i}^{\pm} Z_i^2 \tilde{\sigma}_s(Z_i, E, E_\gamma)}{E_\gamma \beta^2} & E_\gamma \leq E \\ 0 & \text{otherwise} \end{cases}, \tag{67}$$

where E is incoming electron or positron energy, E_γ is the produced photon energy and $\tilde{\sigma}_s(Z_i, E, E_\gamma)$ is the total scaled bremsstrahlung energy-weighted cross-section from interpolation of the Seltzer and Berger [77], given in cm^2. Note that all interpolations in this paper are done using cubic Hermite spline interpolation [78]. These cross-sections are defined for $Z_i \leq 100$ and energies between 1 keV and 10 GeV. The following factor is used [52]

$$\begin{aligned} F_{p,i}^{+} = 1 - \exp\{ & -1.2359 \times 10^{-1} t_i + 6.1274 \times 10^{-2} t_i^2 - 3.1516 \times 10^{-2} t_i^3 + 7.7446 \times 10^{-3} t_i^4 \\ & - 1.0595 \times 10^{-3} t_i^5 + 7.0568 \times 10^{-5} t_i^6 - 1.8080 \times 10^{-6} t_i^7 \}, \end{aligned} \tag{68}$$

with

$$t_i = \ln\left(1 + \frac{10^6 E}{Z_i^2}\right) \tag{69}$$

for positrons, and $F_{p,i}^{-} = 1$ for electrons. This formula for positrons is based on interpolation of the tabulated positron-to-electron ratios from Kim et al. [79]. The double differential cross-sections, for deflected electron, deflected positron or produced photon, are given by [29]

$$\sigma_s^i(E \to E_e, \mu) = \frac{1}{2\pi} \sigma_s^i(E \to E_e) \delta(\mu - 1) \quad \text{and} \quad \sigma_s^i(E \to E_\gamma, \mu) = \frac{1}{2\pi} \sigma_s^i(E \to E_\gamma) \Theta(E, E_\gamma, \mu), \tag{70}$$

where it is assumed, as in CEPXS 1.0 [29], that the incoming electron does not deflect from its trajectory after interaction ($\mu_e = 1$). This implies that the soft momentum transfer value is zero. The bremsstrahlung photon angular distribution, greatly inspired by the modified dipole distribution from Acosta et al. [80,81], is given by

$$\Theta(E, E_\gamma, \mu) = \frac{3(1 - C^2)}{4(2A + B)(1 - \mu C)^2} \left[(A + B) + (A - B) \left(\frac{\mu - C}{1 - \mu C} \right)^2 \right], \tag{71}$$

where the parameters $A = A(E, E_\gamma)$, $B = B(E, E_\gamma)$ and $C = C(E, E_\gamma)$, which have values strictly between 0 and 1, are adjusted by least-square method to fit the shape function from Poškus [82] for $E \leq 3$ MeV, and are set to give the dipole distribution ($A = 1$, $B = 0$ and $C = \beta$) for energy $E > 3$ MeV. This approach is similar to the one used in the PENELOPE code, where a 500 keV threshold is applied rather than 3 MeV [81], and where the shape functions are extracted from Kissel et al. [83] rather than the more recent and comprehensive work from Poškus.

5.1. Scattering cross-sections for deflected electron or positron

The Legendre moments of the differential scattering cross-sections for the produced bremsstrahlung photon are given by

$$\sigma_{s,\ell}^i(E \to E_\gamma) = 2\pi \int_{-1}^{1} d\mu \, P_\ell(\mu) \sigma_s^i(E \to E_\gamma, \mu) = \sigma_s^i(E \to E_\gamma) \Theta_\ell(E, E_\gamma), \tag{72}$$

where the moment of the angular distribution is given by

$$\Theta_\ell(E, E_\gamma) = \int_{-1}^{1} d\mu \, P_\ell(\mu) \Theta(E, E_\gamma, \mu). \tag{73}$$

These Legendre moments of the angular distribution can be computed analytically by expanding the Legendre polynomials in power of μ using Eq. (54) such as

$$\Theta_\ell(E, E_\gamma) = \frac{3(1 - C^2)}{4(2A + B)} \frac{1}{2^\ell} \sum_{k=0}^{\lfloor \ell/2 \rfloor} C_{\ell,k} \left[(A + B) I^{\ell - 2k, 2}(C) + (A - B) \sum_{j=0}^{2} \alpha_j I^{\ell - 2k + j, 4}(C) \right] \tag{74}$$

where $\alpha_0 = C^2$, $\alpha_1 = -2C$ and $\alpha_2 = 1$. The remaining integrals are given by

$$I^{n,m}(a) = \int_{-1}^{1} d\mu \frac{\mu^n}{(1 - a\mu)^m} = \mathcal{G}_3^{n,m}(a, 1) - \mathcal{G}_3^{n,m}(a, -1) \tag{75}$$

and are solved using integral expressions from Gradshteyn et al. (Sect. 2.153) [68]

$$\mathcal{G}_3^{n,m}(a,x) = \begin{cases} -\dfrac{1}{a}\log|1-ax| & n=0 \text{ and } m \neq 1 \\ \dfrac{(1-ax)^{1-m}}{1-m} & n=0 \text{ and } m=1 \\ -\dfrac{1}{a(n-m+1)}\left[(1-ax)^{1-m}x^n - n\mathcal{G}_3^{n-1,m}(a,x)\right] & n>0 \text{ and } n-m\neq -1 \\ -\dfrac{1}{(1-m)}\left[(1-ax)^{1-m}x^{n+1} - (n-m+2)\mathcal{G}_3^{n,m+1}(a,x)\right] & n>0 \text{ and } n-m=-1 \end{cases}. \tag{76}$$

The high-order moment correction is applied for elastic cross-sections (Eq. (60)). The multigroup Legendre moments of the scattering cross-sections are therefore given by

$$\Sigma_{s,\ell,g'}^{\mathrm{e}\pm\to\gamma}(E) = \sum_{i=1}^{N_e} \mathcal{N}_{n,i} f_i \int_{E'_{g+1/2}}^{\min\left\{E'_{g-1/2},E\right\}} dE_\gamma \sigma_{s,\ell}^i(E\to E_\gamma)\mathcal{H}_b\,. \tag{77}$$

This equation is solved using numerical quadrature.

5.2. Catastrophic total cross-sections

The catastrophic bremsstrahlung total cross-sections are defined by

$$\Sigma_t^{\mathrm{e}\pm}(E) = \sum_{i=1}^{N_e} \mathcal{N}_{n,i} f_i \int_0^{E_c(E)} dE_e \sigma_{s,0}^i(E\to E_e) \tag{78}$$

and are solved using numerical quadrature.

5.3. Absorption cross-sections

The bremsstrahlung absorption cross-sections for annihilation calculations are given by

$$\Sigma_a^{\mathrm{brem}}(E) = \sum_{i=1}^{N_e} \mathcal{N}_{n,i} f_i \int_0^{E_{G+1/2}} dE_e \sigma_{s,0}^i(E\to E_e) \tag{79}$$

and are solved using numerical quadrature.

5.4. Total stopping powers

The radiative stopping powers of electrons are given by

$$S_t(E) = \alpha r_e^2 (E+1) \sum_{i=1}^{N_e} \mathcal{N}_{n,i} f_i F_{p,i}^{\pm} Z_i^2 \phi_{\mathrm{rad}}(Z_i,E)\,, \tag{80}$$

where $\phi_{\mathrm{rad}}(Z_i,E)$ are also given by the tables of Selzer and Berger [77].

5.5. Soft stopping powers

The soft radiative stopping powers, $S^{\mathrm{e}\pm}(E)$, are given by removing catastrophic bremsstrahlung stopping powers from total stopping powers. They are given by

$$S^{\mathrm{e}\pm}(E) = S_t(E) - \sum_{i=1}^{N_e} \mathcal{N}_{n,i} f_i \int_0^{E_c(E)} dE_e (E-E_e)\sigma_{s,0}^i(E\to E_e)\,, \tag{81}$$

where the integral is solved with numerical quadrature.

6. Annihilation

The following cross-sections describe the annihilation of an incoming positron ($p' = \mathrm{e}+$) with an atomic electron producing two photons ($p = \gamma$), assuming that the electrons are free and at rest. The differential cross-sections in the energy of the lowest energy photon [47,84]

$$\sigma_s(E \to E_{\gamma_-}) = \frac{\pi r_e^2}{(\gamma+1)^2(\gamma^2-1)} \left[S(\zeta) + S(1-\zeta) \right] \tag{82}$$

with

$$S(\zeta) = -(\gamma+1)^2 + (\gamma^2+4\gamma+1)\frac{1}{\zeta} - \frac{1}{\zeta^2}, \tag{83}$$

where E is the incoming positron energy, E_{γ_-} is the lowest photon energy, $E_{\gamma_+} = E + 2 - E_{\gamma_-}$ is the highest photon energy and $\zeta = E_{\gamma_-}/(E+2)$ is the ratio of the lowest energy photon to the total (kinetic + mass) energy. The value of the lowest photon energy is bounded by

$$E^{\max} = \frac{\gamma+1}{2} \quad \text{and} \quad E^{\min} = \frac{\gamma+1}{\gamma+1+\sqrt{\gamma^2-1}}. \tag{84}$$

The scattering angles of the lowest and highest energy photons are respectively

$$\mu_- = \frac{1}{\sqrt{\gamma^2-1}} \left[\gamma + 1 - \frac{1}{\zeta} \right] \quad \text{and} \quad \mu_+ = \frac{1}{\sqrt{\gamma^2-1}} \left[\gamma + 1 - \frac{1}{1-\zeta} \right], \tag{85}$$

and the double differential cross-sections for the lowest and highest energy photons are given by

$$\sigma_s(E \to E_{\gamma_-}, \mu) = \frac{1}{2\pi}\sigma_s(E \to E_{\gamma_-})\delta(\mu - \mu_-) \quad \text{and} \quad \sigma_s(E \to E_{\gamma_+}, \mu) = \frac{1}{2\pi}\sigma_s(E \to E_{\gamma_+})\delta(\mu - \mu_+). \tag{86}$$

6.1. Scattering cross-sections for the lowest energy photons

The annihilation Legendre moments of the differential scattering cross-sections for the lowest energy photons are given by

$$\sigma_{s,\ell}(E \to E_{\gamma_-}) = 2\pi \int_{-1}^{1} d\mu\, P_\ell(\mu)\sigma_s(E \to E_{\gamma_-}, \mu) = P_\ell(\mu_-)\sigma_s(E \to E_{\gamma_-}). \tag{87}$$

The multigroup Legendre moments of the scattering cross-sections are therefore given by

$$\Sigma_{s,\ell,g'}^{e+\to\gamma}(E) = \sum_{i=1}^{N_e} \mathcal{N}_{n,i} f_i Z_i \int_{\max\left\{E_{g+1/2}^{\gamma}, E^{\min}\right\}}^{\min\left\{E_{g-1/2}^{\gamma}, E^{\max}\right\}} dE_{\gamma_-}\, \sigma_{s,\ell}(E \to E_{\gamma_-})\mathcal{H}_b. \tag{88}$$

This equation is solved using numerical quadrature.

6.2. Scattering cross-sections for the highest energy photons

The annihilation Legendre moments of the differential scattering cross-sections for the highest energy photons are given by

$$\sigma_{s,\ell}(E \to E_{\gamma_+}) = 2\pi \int_{-1}^{1} d\mu\, P_\ell(\mu)\sigma_s(E \to E_{\gamma_+}, \mu) = P_\ell(\mu_+)\sigma_s(E \to E_{\gamma_+}). \tag{89}$$

The multigroup Legendre moments of the scattering cross-sections are therefore given by

$$\Sigma_{s,\ell,g'}^{e+\to\gamma}(E) = \sum_{i=1}^{N_e} \mathcal{N}_{n,i} f_i Z_i \int_{\max\left\{E_{g+1/2}^{\gamma}, E^{\max}\right\}}^{\min\left\{E_{g-1/2}^{\gamma}, (\gamma+1)-E^{\min}\right\}} dE_{\gamma_+}\, \sigma_{s,\ell}(E \to E_{\gamma_+})\mathcal{H}_b. \tag{90}$$

This equation is solved using numerical quadrature.

6.3. Total cross-sections

The annihilation total cross-sections are defined by

$$\Sigma_t^{e+}(E) = \sum_{i=1}^{N_e} \mathcal{N}_{n,i} f_i Z_i \int_{E^{\min}}^{E^{\max}} dE_{\gamma_-}\, \sigma_{s,0}(E \to E_{\gamma_-}) \tag{91}$$

and are solved analytically.

6.4. Annihilation when positrons scatter under the cutoff energy

Positrons ($p' = \texttt{e+}$) annihilate with atomic electrons and produce two photons ($p = \gamma$). Therefore, all positrons scattered under the cutoff energy $E_{G+1/2}$ have to annihilate. The positron energy under the cutoff is small enough that the annihilation photon can be assumed to have isotropic scattering as in GEANT4 [85]. We also assume that two 511 keV photons are produced. The positrons are scattered under the cutoff following either an inelastic interaction or a bremsstrahlung interaction, and positrons can also be produced under the cutoff following pair production interaction. The $\ell = 0$ Legendre moments of the scattering cross-sections are given by

$$\Sigma^{\texttt{e+}\to\gamma}_{s,0,g'\to g} = 2\left[\Sigma^{\texttt{inel}}_{a,g'} + \Sigma^{\texttt{brem}}_{a,g'}\right] \times \begin{cases} 1 & 1 \in [E'_{g+1/2}, E'_{g-1/2}] \\ 0 & \text{otherwise} \end{cases} \tag{92}$$

and

$$\Sigma^{\gamma\to\gamma}_{s,0,g'\to g} = 2\Sigma^{\texttt{pp}}_{a,g'} \times \begin{cases} 1 & 1 \in [E'_{g+1/2}, E'_{g-1/2}] \\ 0 & \text{otherwise} \end{cases}, \tag{93}$$

where the absorption cross-sections are given by integration of Eqs. (34), (79) and (127) over group g' and where the $\ell \geq 1$ moments are equal to zero since scattering is isotropic.

7. Rayleigh scattering

The Rayleigh cross-sections, which described the elastic scattering of photons ($p = p' = \gamma$), are given by [86]

$$\sigma^i_s(E,\mu) = \pi r_e^2 \left(1+\mu^2\right)\left[\left(F_i(E,\mu) + f'_i(E)\right)^2 + \left(f''_i(E)\right)^2\right], \tag{94}$$

where $F_i(E,\mu)$ is the atomic form factor for the i^{th}-element, where the factors $f'_i(E)$ and $f''_i(E)$ are respectively the real and imaginary parts of the anomalous scattering factors for the i^{th}-element, which are all tabulated by the Japanese evaluated nuclear data library (JENDL-5) [87], which are based on the EPDL library [88]. The double differential cross-sections are given by

$$\sigma^i_s(E \to E', \mu) = \sigma^i_s(E,\mu)\delta(E' - E). \tag{95}$$

7.1. Scattering cross-sections of the incoming photon

The Rayleigh Legendre moments of the differential scattering cross-sections of the incoming photon are given by

$$\Sigma^{\gamma\to\gamma}_{s,\ell}(E) = \sum_{i=1}^{N_e} \mathcal{N}_{n,i} f_i \int_{-1}^{1} P_\ell(\mu)\sigma^i_s(E,\mu), \tag{96}$$

which are solved using numerical quadrature.

7.2. Total cross-sections

The Rayleigh total cross-sections are given by

$$\Sigma^{\gamma}_{s,\ell}(E) = \Sigma^{\gamma\to\gamma}_{s,0}(E). \tag{97}$$

8. Compton scattering

The Compton cross-section describes the interaction of an incoming photon ($p' = \gamma$) with atomic electrons, resulting in a scattered photon ($p = \gamma$) and a produced electron ($p = \texttt{e+}$). The Klein-Nishina differential cross-section in the energy of the scattered photon, for a single interaction with an assumed free atomic electron, is given by [29,84]

$$\sigma_s(E \to E') = \frac{\pi r_e^2}{E^2}\left[\frac{E}{E'} + \frac{E'}{E} - 2\left(\frac{1}{E'} - \frac{1}{E}\right) + \left(\frac{1}{E'} - \frac{1}{E}\right)^2\right], \tag{98}$$

where E is the incoming photon energy, E' is the scattered photon energy and $W = E - E'$ is the produced electron energy. The scattering angles for the scattered photon and the produced electron are respectively

$$\mu_\gamma = 1 + \frac{1}{E} - \frac{1}{E'} \quad \text{and} \quad \mu_e = \frac{1+E}{E}\left[1 + \frac{2}{W}\right]^{-\frac{1}{2}}. \tag{99}$$

The double differential cross-sections for the scattered photon and the produced electron, with an incoherent scattering factor $S_i(E,\mu)$ extracted from JENDL-5 library [87] taking into account some binding effects [89], are given by

$$\sigma_s^i(E \to E', \mu) = \frac{1}{2\pi} S_i(E, \mu) \sigma_s(E \to E') \delta(\mu - \mu_\gamma) \tag{100}$$

and

$$\sigma_s^i(E \to W, \mu) = \frac{1}{2\pi} S_i(E, \mu) \sigma_s(E \to W) \delta(\mu - \mu_e) . \tag{101}$$

8.1. Scattering cross-sections of the incoming photon

The Compton Legendre moments of the differential scattering cross-sections of the incoming photon are given by

$$\sigma_{s,\ell}^i(E \to E') = 2\pi \int_{-1}^{1} d\mu \, P_\ell(\mu) \sigma_s^i(E \to E', \mu) = P_\ell(\mu_\gamma) S_i(E, \mu_\gamma) \sigma_s(E \to E') . \tag{102}$$

The multigroup Legendre moments of the scattering cross-sections are therefore given by

$$\Sigma_{s,\ell,g'}^{\gamma \to \gamma}(E) = \sum_{i=1}^{N_e} \mathcal{N}_{n,i} f_i \int_{\max\left\{E'_{g+1/2}, \frac{E}{1+2E}\right\}}^{\min\left\{E'_{g-1/2}, E\right\}} dE' \sigma_{s,\ell}^i(E \to E') , \tag{103}$$

which are solved by numerical quadrature.

8.2. Scattering cross-sections of the produced electron

The Compton Legendre moments of the differential scattering cross-sections of the produced electron are given by

$$\sigma_{s,\ell}^i(E \to W) = 2\pi \int_{-1}^{1} d\mu \, P_\ell(\mu) \sigma_s^i(E \to W, \mu) = P_\ell(\mu_e) S_i(E, \mu_e) \sigma_s(E \to W) . \tag{104}$$

The multigroup Legendre moments of the scattering cross-sections are therefore given by

$$\Sigma_{s,\ell,g'}^{\gamma \to \mathrm{e}^-}(E) = \sum_{i=1}^{N_e} \mathcal{N}_{n,i} f_i \int_{E'_{g+1/2}}^{\min\left\{E'_{g-1/2}, \frac{2E^2}{1+2E}\right\}} dW \sigma_\ell^i(E \to W) , \tag{105}$$

which are solved by numerical quadrature.

8.3. Total cross-sections

The Compton total cross-sections are defined by

$$\Sigma_t^\gamma(E) = \sum_{i=1}^{N_e} \mathcal{N}_{n,i} f_i \int_{\frac{E}{1+2E}}^{E} dE' \, S_i(E, \mu_\gamma) \sigma_{s,0}(E \to E') , \tag{106}$$

which are solved by numerical quadrature.

9. Photoelectric effect

The photoelectric cross-section describes the absorption of an incoming photon ($p' = \gamma$) and the emission of an atomic electron ($p = \mathrm{e}^-$). The microscopic absorption cross-sections are given by

$$\sigma_a^i(E) = \sum_{k=1}^{N_{\mathtt{shells}}} \sigma_a^{i,k}(E) , \tag{107}$$

where $\sigma_a^{i,k}(E)$ is given by linear interpolation of the data given by the absorption cross-sections per subshells from the JENDL-5 library [87], which are available for $Z_i \leq 100$ and for energies up to 100 GeV.

9.1. Scattering cross-sections of the produced electron

The photoelectric scattering cross-sections are given by

$$\sigma_s^{i,k}(E \to E', \mu) = \sigma_a^{i,k}(E)\delta(E' - E + U_{i,k})\Theta(E, \mu), \tag{108}$$

where E' is the energy of the photo-electron, $U_{i,k}$ is the binding energy of the k$^{\text{th}}$ shell and the Sauter cross-section for the K-shell, normalized over the angular domain, is given by [90]

$$\Theta(E, \mu) = \Gamma(E)\frac{1-\mu^2}{(1-\beta\mu)^4}\left[1 + \frac{\gamma(\gamma-1)(\gamma-2)}{2}(1-\beta\mu)\right], \tag{109}$$

where the normalization factor is

$$\Gamma(E) = \left\{\frac{4}{3(1-\beta^2)^2} + \frac{\gamma(\gamma-1)(\gamma-2)}{2\beta^3}\left[\frac{2\beta}{1-\beta^2} - \ln\left(\frac{1+\beta}{1-\beta}\right)\right]\right\}^{-1}. \tag{110}$$

The Legendre moments of the normalized Sauter cross-section are given by

$$\Theta_\ell(E) = \int_{-1}^{1} d\mu P_\ell(\mu)\Theta(E, \mu). \tag{111}$$

The Legendre moments are computed analytically by expanding the Legendre polynomials in power of μ using Eq. (54) such as

$$\Theta_\ell(E) = \frac{\Gamma(E)}{2^\ell}\sum_{k=0}^{\lfloor \ell/2 \rfloor} C_{\ell,k}\sum_{j=0}^{1}(-1)^j\left[I^{\ell-2k+2j,4}(\beta) + \frac{\gamma(\gamma-1)(\gamma-2)}{2}I^{\ell-2k+2j,3}(\beta)\right] \tag{112}$$

where the integrals are given by Eq. (75). The high-order moment correction is applied for elastic cross-sections (Eq. (60)). The scattering cross-sections are given by

$$\Sigma_{s,\ell,g'}^{\gamma\to \mathtt{e}^-}(E) = \sum_{i=1}^{N_e}\mathcal{N}_{n,i}f_i\int_{E'_{g+1/2}}^{E'_{g-1/2}} dE' \sum_{k=1}^{N_{\mathtt{shells}}}\sigma_{s,\ell}^{i,k}(E \to E'), \tag{113}$$

which can be rewritten as

$$\Sigma_{s,\ell,g'}^{\gamma\to \mathtt{e}^-}(E) = \sum_{i=1}^{N_e}\mathcal{N}_{n,i}f_i\sum_{k=1}^{N_{\mathtt{shells}}}\sigma_a^{i,k}(E)\Theta_\ell(E) \times \begin{cases} 1 & E - U_{i,k} \in [E'_{g+1/2}, E'_{g-1/2}] \\ 0 & \text{otherwise} \end{cases}. \tag{114}$$

9.2. Total cross-sections

The photoelectric total cross-sections are simply

$$\Sigma_t^\gamma(E) = \sum_{i=1}^{N_e}\mathcal{N}_{n,i}f_i\sigma_a^i(E). \tag{115}$$

10. Pair production

The pair production cross-section describes the absorption of a photon ($p' = \gamma$) and the production of an electron ($p = \mathtt{e}^-$) and a positron ($p = \mathtt{e}^+$). A variation of the semi-empirical model of Baró [91] is used and, in a monoelemental material i, the differential cross-section is given by

$$\sigma_s^i(E \to E') = \begin{cases} A(Z_i, E)\left[2\left(\frac{1}{2} - \frac{E'+1}{E}\right)^2\phi_{i,1}(E') + \phi_{i,2}(E')\right] & E > 2 \\ 0 & \text{otherwise} \end{cases}, \tag{116}$$

where E is the incoming photon energy and E' is the outgoing electron or positron energy. The screening functions, derived from the one of Tsai [92], are given by

$$\phi_{i,1}(E') = \max\left\{g_{i,1}(E') + g_{i,0}, 0\right\} \quad \text{and} \quad \phi_{i,2}(E') = \max\left\{g_{i,2}(E') + g_{i,0}, 0\right\}, \tag{117}$$

where

$$g_{i,1}(E') = \frac{7}{3} - 2\ln(1+b_i^2) - 6b_i \arctan\left(\frac{1}{b_i}\right) - b_i^2\left[4 - 4b_i \arctan\left(\frac{1}{b_i}\right) - 3\ln\left(1+\frac{1}{b_i^2}\right)\right],$$
$$g_{i,2}(E') = \frac{11}{6} - 2\ln(1+b_i^2) - 3b_i \arctan\left(\frac{1}{b_i}\right) - \frac{b_i^2}{2}\left[4 - 4b_i \arctan\left(\frac{1}{b_i}\right) - 3\ln\left(1+\frac{1}{b_i^2}\right)\right], \tag{118}$$

$$g_{i,0} = 4\ln(r_{s,i}) - 4f_{C,i}\,, \tag{119}$$

with

$$b_i = \frac{r_{s,i}}{2}\frac{E}{(E'+1)(E-E'-1)}\,. \tag{120}$$

The variable $r_{s,i}$ corresponds to the reduced screening radius, tabulated in Baró [91] for $Z_i \leq 92$ and extended up to $Z_i \leq 99$ in PENELOPE [7]. The high-energy Coulomb correction $f_{C,i}$ is given by [93]

$$f_{C,i} = \alpha^2 Z_i^2 \sum_{k=1}^{\infty} \frac{1}{k(k^2+\alpha^2 Z_i^2)}\,. \tag{121}$$

As it is done in EGSnrc [8], a normalization factor $A(Z_i, E)$ is added to the pair production cross-section, which is defined as the ratio between the total cross-sections obtained with $A(Z_i, E) = 1$ and the tabulated values from JENDL-5 for the pair production in both the nuclear and electron field [87]

$$A(Z_i, E) = \frac{\sigma_t^{\text{JENDL-5}}(Z_i, E)}{\sigma_t(Z_i, E)\big|_{A=1}}\,. \tag{122}$$

Since pair production and bremsstrahlung are closely related through a substitution rule, the same angular distribution can be used for the electron and positron emission [29,92]. The double differential cross-section is given by

$$\sigma_s^i(E \to E', \mu) = \frac{1}{2\pi}\sigma_s^i(E \to E')\Theta(E, \mu)\,. \tag{123}$$

This distribution $\Theta(E, \mu)$ is defined by Eq. (71).

10.1. Scattering cross-sections for the produced electron and positron

The pair production Legendre moments of the differential scattering cross-sections for the produced leptons are given by

$$\sigma_{s,\ell}^i(E \to E') = 2\pi \int_{-1}^{1} d\mu\, P_\ell(\mu)\sigma_s^i(E \to E', \mu) = \sigma_s^i(E \to E')\Theta_\ell(E)\,, \tag{124}$$

where the values of $\Theta_\ell(E)$ are given by Eq. (73). The multigroup Legendre moments of the scattering cross-sections are therefore given by

$$\Sigma_{s,\ell,g'}^{\gamma\to e^\pm}(E) = \sum_{i=1}^{N_e} \mathcal{N}_{n,i} f_i \int_{E'_{g+1/2}}^{\min\left\{E'_{g-1/2}, E-2\right\}} dE_e \sigma_{s,\ell}^i(E \to E')\mathcal{H}_b\,, \tag{125}$$

which are solved by numerical quadrature.

10.2. Total cross-sections

The pair production total cross-sections are defined by

$$\Sigma_t^\gamma(E) = \sum_{i=1}^{N_e} \mathcal{N}_{n,i} f_i \int_0^{E-2} dE' \sigma_{s,0}^i(E \to E')\mathcal{H}_b \tag{126}$$

and are solved using numerical quadrature.

10.3. Absorption cross-sections

The pair production absorption cross-sections, which are required for annihilation calculations, are given by

$$\Sigma_a^{pp}(E) = \sum_{i=1}^{N_e} \mathcal{N}_{n,i} f_i \int_0^{\min\left\{E-2, E_{G+1/2}\right\}} dE' \sigma_{s,0}^i(E \to E')\mathcal{H}_b \tag{127}$$

and are solved using numerical quadrature.

11. Atomic relaxation

The ionization of an atomic electron in the k^{th} shell, by incoming particle, leaves behind a vacancy in the electronic structure of the atom i. Such vacancy in an inner shell of the atom is filled in by an outer-shell electron, resulting either by the emission of a fluorescence photon or by the ejection of a valance electron called an Auger electron, leaving additional vacancies in the outer shell, which also results in the production of photon or electron and so on. These intricate relaxation processes are often referred to as relaxation cascades, for which a simplified visual diagram can be found in Lorence et al. [29] and Naceur et al. [34]. Because such calculation can be rather intensive for high-Z atom, for this work, only particle productions with probability of occurrence, following an initial ionization event, that is greater than 0.1% are included. Finally, only the N_t specific electron cascade transitions which result in electron or photon with energy greater than the cutoff energy $E_{G+1/2}$ are kept for the following calculations.

The differential cross-sections corresponding to the production of either fluorescence ($p' = \gamma$) or Auger electron ($p' = \mathrm{e}^-$) following a specific electron cascade transition j, where $1 \leq j \leq N_t$, with the produced particle energy, $\Delta E_{i,k,j}$, and the probability of occurrence of the j electron cascade, $\eta^{p'}_{i,k,j}$, is given by

$$\sigma_s^{i,k,j,p\to p'}(E \to E') = \eta^{p'}_{i,k,j}\delta(E' - \Delta E^{p'}_{i,k,j})\sigma_t^{i,k,p}(E), \tag{128}$$

where $\sigma_t^{i,k,p}(E)$ is the k^{th}-shell cross-sections of either inelastic electron ($p = \mathrm{e}^-$), inelastic positron ($p = \mathrm{e}^+$) or photoelectric interaction ($p = \gamma$) given in previous sections. Contrary to CEPXS 1.0, the relaxation is correlated with the inelastic model [29]. The values of $\Delta E^{p'}_{i,k,j}$ and $\eta^{p'}_{i,k,j}$ are computed using the relaxation data from the JENDL-5 library [87], based on the EADL library [48], as proposed by Hébert and Naceur [35]. The production of fluorescence photon and Auger electron is assumed to be isotropic.

11.1. Scattering cross-sections of produced Auger electron or fluorescence photon

The relaxation $\ell = 0$ Legendre moments of the differential scattering cross-sections of the produced Auger electron or fluorescence photon are given by

$$\sigma_{s,0,g'}^{i,p\to p'}(E) = \sum_{k=1}^{N_{\texttt{shells}}} \sigma_t^{i,k,p}(E) \sum_{j=1}^{N_t} \eta^{p'}_{i,k,j} \int_{E'_{g+1/2}}^{E'_{g-1/2}} dE' \delta(E' - \Delta E^{p'}_{i,k,j}), \tag{129}$$

where the $\ell \geq 1$ moments are equal to zero since scattering is isotropic. The resulting cross-section is given by

$$\Sigma_{s,0,g'}^{p\to p'}(E) = \sum_{i=1}^{N_e} \mathcal{N}_{n,i} f_i \sum_{k=1}^{N_{\texttt{shells}}} \sigma_t^{i,k,p}(E) \sum_{j=1}^{N_t} \eta^{p'}_{i,k,j} \times \begin{cases} 1 & \Delta E^{p'}_{i,k,j} \in [E'_{g+1/2}, E'_{g-1/2}] \\ 0 & \text{otherwise} \end{cases}. \tag{130}$$

12. Results and discussion

12.1. Comparison between Boltzmann Fokker-Planck and Monte-Carlo calculations

The energy spectrum per particle and the energy deposition profile calculated with RADIANT will be compared to the energy spectrum obtained with Monte Carlo calculations. Such results offer a comprehensive overview of its algorithms' performance and limitations. We are considering normally incident electron and photon beams on water (H_2O), aluminum (Al) and gold (Au). The incident beam has energies of 1 MeV, 10 MeV and 100 MeV, which correspond respectively to Fig. 2, Fig. 3 and Fig. 4.

The spatial domain, along the principal axis, is two times the range of electrons in the material at the incident beam energy, while the transverse size is assumed to be infinite. The resulting geometry is a 1D slab, where particles are restricted to move along a single spatial dimension but can still travel in various directions relative to the slab's surface. This assumption greatly simplifies the Boltzmann Fokker-Planck transport equation (see [44]) and reduces the sources of error related to multidimensional transport with discrete ordinates solver [34]. The spatial domain is divided into 80 equal-size voxels. The energy domain is split into 80 logarithmically spaced energy groups, where the mean energy E_1 of the most energetic group is the incident beam energy, and the cutoff energy is given by $E_{G+1/2} = 1$ keV, which is the lower validity bound of RADIANT algorithms. To deal with the derivative in space and energy, a 3rd-order accurate coupled space-energy discontinuous Galerkin scheme [94–96]. For angular discretization, the discrete ordinates' method with Galerkin quadrature methodology, as developed by Morel [20], is used. Galerkin quadratures ensure that, whatever choice of quadrature is made to discretize the angular domain, forward-peaked scattering will be treated accurately [21,97]. Since the beam under consideration is normally incident, the choice was made to utilize a 16-point Gauss-Lobatto quadrature, as it incorporates an integration point along $\mu = 0$. Galerkin quadrature has a restriction concerning the Legendre order, which has to be $L = 15$. We are extracting the forward-peaked part of the elastic scattering from the scattering cross-sections and transferring it to the momentum transfer term [70]. The angular Fokker-Planck term, which deals with the momentum transfer, is treated using a finite-difference approach which ensures 2nd order accurate, positive and monotone treatment of forward scattering [73].

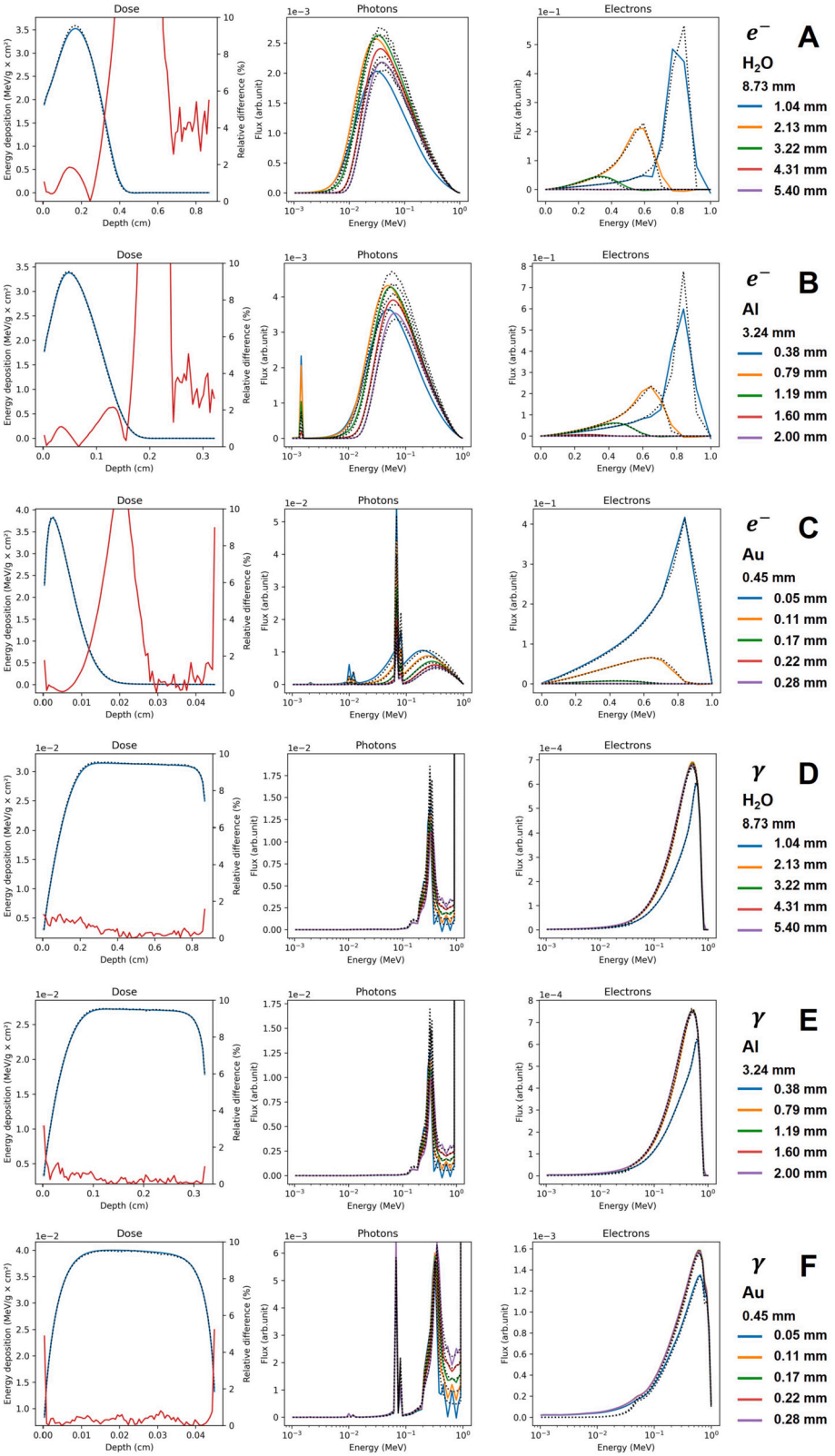

Fig. 2. Dose and energy spectrum per particle for normally incident 1 MeV electron and photon beams on water, aluminum and gold. Black curves are from GEANT4, while coloured curves are from our deterministic Boltzmann Fokker-Planck algorithms. The length of the slab is indicated on the right, as well as the depth at which each energy spectrum curves are extracted. Relative differences in dose deposition are given in red.

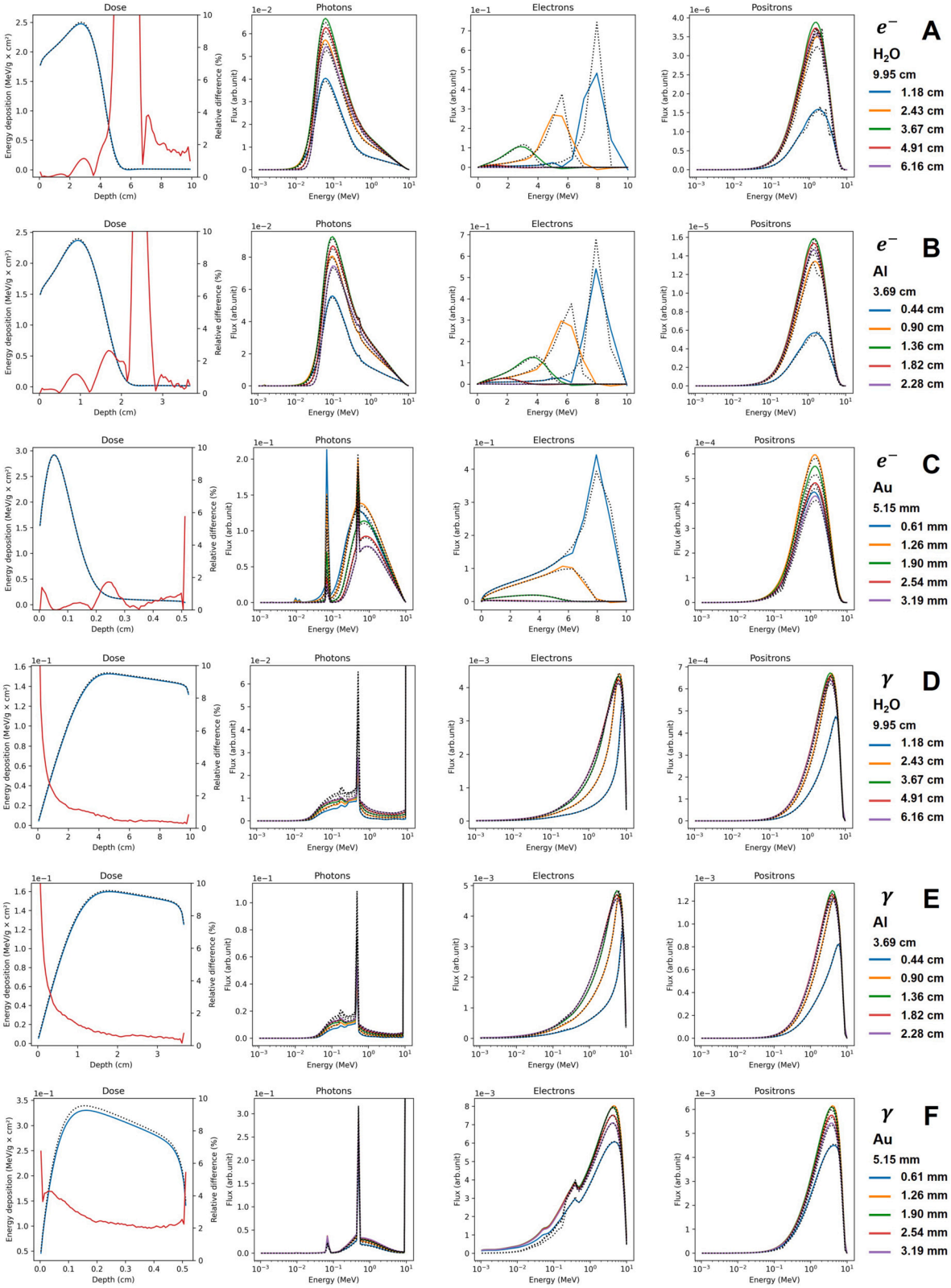

Fig. 3. Dose and energy spectrum per particle for normally incident 10 MeV electron and photon beams on water, aluminum and gold.

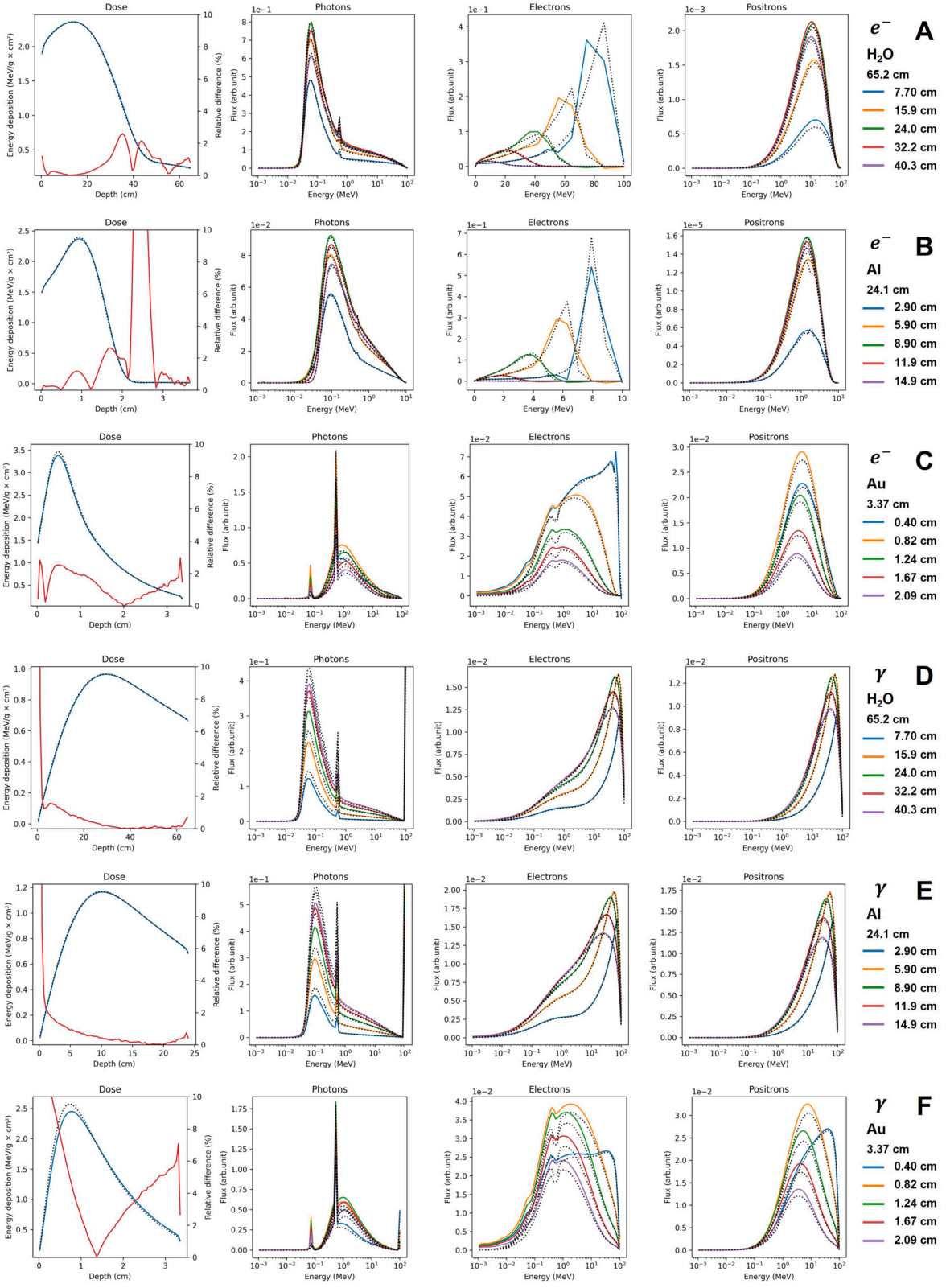

Fig. 4. Dose and energy spectrum per particle for normally incident 100 MeV electron and photon beams on water, aluminum and gold.

The reference Monte Carlo solutions are obtained from GEANT4 (v11.0.1) [4,5], using G4EmPenelope constructor [7], based on PENELOPE physics models, which are widely recognized as a state-of-the-art for electron, positron and photon transport. To extract the energy spectrum in GEANT4, the occurrence of a type of particle in an energy group and a voxel is counted and saved in a matrix $\mathcal{M}$ of size $3 \times 80 \times 80$. At each step of particle interaction and transport, the particle's kinetic energy and its pre- and post-step positions are measured. Then, for each voxel j the particle crosses, for the particle i with kinetic energy in energy group k, the particle travel length during the step, divided by the total number of voxels crossed by the particle, is added to the matrix element $\mathcal{M}_{i,j,k}$. For calculations, 100 million incident particles are simulated for 1 MeV and 10 MeV beams and 10 million for 100 MeV ones. Scoring cells of the same size as the discretized space and energy domains of RADIANT deterministic algorithms and the same 1 keV cutoff are used. While the transverse width cannot be set to infinity in GEANT4, setting 100 meters width, which is exceedingly greater than the electron range, practically gives the same results.

First, a Monte Carlo solution's numerical limitation must be emphasized. For electrons or positrons, in their energy spectrum curves at a specific energy, the Monte Carlo curves exhibit a sudden drop, while RADIANT curves remain smooth and regular. This discrepancy is evident in the electron spectrum depicted in Fig. 2F around 50 keV or Fig. 3F around 100 keV. The reason behind this difference lies in the modelling choices of the PENELOPE algorithm, as implemented in GEANT4, which opts not to generate knock-on electrons below a specific threshold [85]. This method is typical of mixed, or class II, Monte Carlo algorithms [7,98], which distinguishes between soft and catastrophic scattering events. In contrast, the knock-on energy cutoff in RADIANT is set at the cutoff energy $E_{G+1/2}$ and the methodology outlined by Karakow [66] is adopted to ensure compatibility between the elastic model and this choice of cutoff to avoid double counting issues. Consequently, RADIANT transports low-energy knock-on electrons and the particles they produce upon interaction with matter, potentially resulting in differences in particle distribution at low energies. Otherwise, the Monte Carlo energy spectrum curves should accurately represent the particles' distribution in the medium.

A brief examination of the energy spectrum per particle at different depths is sufficient to recognize that RADIANT estimations of the energy distribution of every particle species in any depth in the material are similar to the Monte Carlo ones. RADIANT energy deposition profiles remain also pretty close to the Monte Carlo ones, with a relative difference of more or less 2%, except in a few cases. Discrepancies between the results of the deterministic and Monte-Carlo methods are discussed in the following paragraphs. These results clearly show the potential of discrete ordinates solver for general-purpose coupled photon-electron-positron transport.

For energy deposition, the most obvious deviation from reference is the relative difference peak between the maximum of the dose curve and the bremsstrahlung tail for electrons beams (Fig. 2, A to C, and Fig. 3, A to B), which is more dominant at low Z and low energy. This error is solely caused by the coupled space-energy discretization of the BFP equation, which struggles with the highly varying solution in space and energy that occurs with charged particle transport, and not by the cross-sections models and their discretization [72,96]. The discontinuous Galerkin schemes underestimate the dose in that region and even produce negative energy deposition values. This is due to the nonphysical oscillations of the scheme when it tries to replicate the very sharp peaks of the electron energy spectrums, which results in negative flux dips in the high-energy side of the peaks. For example, it can be observed that deterministic electron energy spectrums in Fig. 3A struggle to replicate Monte-Carlo ones, showing a negative flux dip at the right of the peaks and oscillatory behaviour at their left. This error could be diminished by increasing the number of voxels and energy groups or by employing higher-order coupled space-energy schemes [44,99], which would improve the replication of the peaks, while full mitigation of this error will require innovative work, such as using adaptive schemes [96].

For 1 MeV electron beams (Fig. 2, A to C), significant relative differences can be seen in the tail of the curve. These disparities are related to the interaction that results in energy deposition that far in the medium, mostly by the electron produced by bremsstrahlung photons. The photon spectrum shows that RADIANT curves don't match the reference ones, and while this difference could be attributed to the photon interaction, they seem to perform well in incoming photon benchmark (Fig. 2, D to F), besides the oscillatory behaviour which will be explained shortly. The origin of the discrepancies is likely related to the production of bremsstrahlung photons, but we failed to isolate its root cause. Both PENELOPE and EGSnrc documentations recommend using and use, an interpolation table with increased granularity compared to the one of the Seltzer and Berger [77,81] and use interpolation methods that differ from the cubic Hermite spline method [78]. RADIANT angular distribution is based on the tables of Poškus [82], which is also used in the GEANT4 implementation of PENELOPE [100], rather than the more scarce tables of Kissel et al. [83]. Further investigations will be required to assess the quality of the bremsstrahlung emission modelization of both RADIANT and GEANT4.

For 1 MeV photon beams (Fig. 2 D to F), the photon spectrum shows nonphysical oscillation and even negativities. It is known that the integration of Klein-Nishina Legendre moments is a challenging task due to catastrophic cancellations [101] and, while suitable Legendre moments are enforced by setting higher moments upper bounds, further work will be required to get rid of these artifacts. Nonetheless, while adding a Waller-Hartree incoherent scattering factor to the Klein-Nishina helps consider bindings effects, it omits Doppler broadening and its consequences on angular deviation and energy loss. Brusa et al. [89] proposed a relativistic impulse approximation description of Compton scattering, which formulation is subshell-based like the photoelectric or inelastic model, and such model is implemented in state-of-the-art Monte Carlo code such as PENELOPE and EGSnrc. The generation of Legendre moments for these cross-sections presents a significant challenge, as it requires performing two difficult integrations—over the angle and energy of the scattered photon—successively, with both accuracy and speed. Given that such a model is implemented, relaxation could be directly correlated with Compton ionization in the same way presented in this work.

The pair production models could also be greatly improved if provided with tables similar to the one of Bremsstrahlung rather than the proposed approximate analytic model normalized by tabulated total cross-sections [102]. Moreover, explicit triplet production cross-sections, rather than treating it as pair production as it is done in this work, would be preferable to the current approach since such a phenomenon results in an electron ionization event and subsequent relaxation cascades.

In the energy spectrum, the location of the fluorescence and Auger electron production peaks and the annihilation peaks at 511 keV correspond to the Monte Carlo reference ones. Note that the relaxation peaks, especially the annihilation peak, overestimate the particle production compared to Monte Carlo. This overshooting should be expected because the high Monte Carlo knock-on electron cutoff decreases the low-energy electron contribution to relaxation processes. For the annihilation peak, there is a blind spot. The rate of positrons that scatter under the cutoff energy is estimated using the catastrophic impact ionization and bremsstrahlung cross-sections. However, it neglects that an important source of annihilation photon comes from positrons continuously slowing down to the cutoff energy. With the actual models, these soft positron annihilation following a Bremsstrahlung interaction can be accurately calculated using the catastrophic model to compute the corresponding soft absorption of positrons, but not for impact ionization. For this interaction, which produces the vast majority of such positrons, a major improvement would be to develop an accurate soft absorption cross-section for positrons in the same way soft stopping powers are produced independently from the catastrophic models that are imprecise for small energy losses. Then, the annihilation photon production is underestimated, resulting in a local deposit of energy and charge rather than transporting that energy and charge further via annihilation photons.

Elastic cross-sections at low energies should be investigated more. GEANT4, using the G4EmPenelope constructor, uses Urban's model of multiple scattering under 100 MeV and a mixed scattering model over 100 MeV, which was shown to be less accurate than both EGSnrc and PENELOPE approach [103]. Since the deterministic model is based on the EGSnrc approach, the GEANT4 reference may be less accurate than RADIANT. Nonetheless, the Riley model in CEPXS is likely more accurate than the Mott model with Seltzer correction, but it does not contain the Kawrakow correction to avoid double counting issues with knock-on electrons. Evaluating the exactness of the elastic model and its compatibility with the knock-on electron model is more challenging than it seems, but it should be done.

As for the impact ionization model, while the stopping power should be very accurate for energies down to 1 keV, the catastrophic models could be improved further. These models, while considering binding energies, are based on Møller and Bhabha cross-sections, which are theoretical models for impact ionization with free electrons, neglecting any screening effect due to the atom's electronic structure. These become increasingly inaccurate in representing inner-shell ionization, notably in high-Z atoms like gold. Bote et al. [104,105] have proposed interpolation formula and data, based on the mixed uses of the relativistic plane-wave and distorted-wave Born approximation, for inner-shells ionization. Implementing such a model should be considered to improve impact ionization cross-sections and provide a soft absorption cross-section for positrons, allowing for more accurate estimation of annihilation photon production. It could also provide accurate group-averaged soft momentum transfers for impact ionization, which are assumed to be neglectable in this work.

Some important topics were not covered in the present work. We have only considered a homogeneous medium, not because RADIANT cannot deal with a heterogeneous medium but because this work focuses on cross-section and stopping power production. The BFP equation is efficient in dealing with heterogeneous medium; see [28,34,44] for example. A more significant concern is the ability to deal accurately with determinist radiation transport in a medium which does not exhibit 1D slab geometry. There are additional challenges when dealing with multidimensional geometries with discrete ordinates solvers, notably relating to the angular discretization, such as the requirement to use Galerkin quadrature [20,21], the choice of a subspace of spherical harmonics [97] and scattering positivity [72]. These critical shortcomings will be addressed in subsequent publications. Still, since the multigroup cross-sections developed in this paper depends solely on the direction cosine μ, and never on the azimuthal angle, they can be used directly in multidimensional calculations.

12.2. Comparison between Boltzmann Fokker-Planck calculations and experimental data

To further establish the performance of the proposed physics models, energy and charge deposition profiles from incident electron beams for different materials and energies are compared with experimental data. For the following comparison, the spatial domain, along the principal axis, is 1.2 times the depth of the last experimental data, while the transverse size is assumed to be infinite. The spatial domain is divided into 80 equal-size voxels. The energy domain is divided into 80 logarithmically spaced energy groups, where the mean energy E_1 of the most energetic group is the incident beam energy, and the cutoff energy is given by $E_{G+1/2} = 1$ keV, which is the lowest energy bound available by the developed models. To deal with the derivative in space and energy, a 3^{rd}-order accurate discontinuous Galerkin coupled space-energy scheme is employed. For angular discretization, the discrete ordinates method with Galerkin quadrature methodology. Since the beam under consideration is normally incident, the choice was made to utilize a 14-point Gauss-Lobatto quadrature, as it incorporates an integration point along $\mu = 0$.

Lockwood et al. [106] has produced an extensive set of experimental energy deposition measurements. That work gives such measurements in beryllium, carbon, aluminum, iron, copper, molybdenum, tantalum and uranium for electron beams of 58 keV to 1.033 MeV. The energy deposition results are shown in Fig. 5.

Tabata et al. [108] gives experimental measurements of charge deposition in beryllium, aluminum, copper, silver and gold for electron beams of 4.09 MeV, 7.79 MeV, 11.5 MeV, 14.9 MeV and 23.5 MeV. However, these values are given as the net charge deposited to the total charge of the absorbed electrons, not as the net charge deposited to the total charge of the incident electrons. The following equation can be used to convert between the two definitions [108]

$$C^{\text{incident electrons}}(Z,x,E) = \Big[1 - \eta(Z,E)\Big]\, C^{\text{absorbed electrons}}(Z,x,E) \tag{131}$$

where Z is the atomic number, x is the depth, E is the kinetic energy of the incident electron and $\eta(Z,E)$ is the backscattering coefficient. Tabata et al. [109] proposed an empirical equation to compute backscattering coefficients for $Z \geq 6$. This equation is

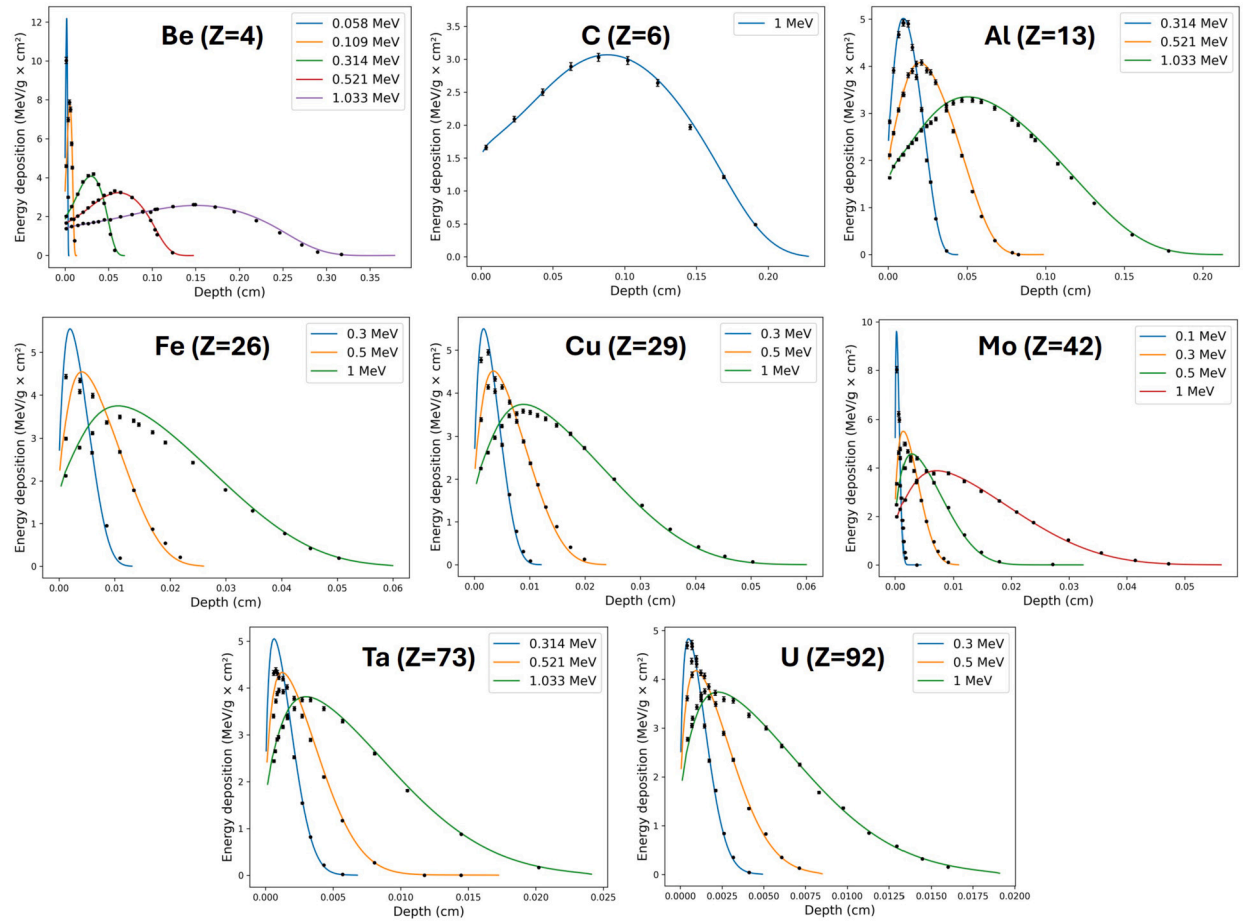

Fig. 5. Energy deposition for normally incident electron beams on beryllium, carbon, aluminum, iron, copper, molybdenum, tantalum and uranium. The experimental data comes from Lockwood et al. [106].

used for all materials but beryllium ($Z = 4$), for which backscattering coefficients are extracted from tables in [108,107]. The charge deposition results are shown in Fig. 6.

Overall, these results show that the proposed physics models and the coupled photon-electron-positron discrete ordinates solver can reproduce experimental energy and charge deposition profiles rather accurately. While the quality of the results in some materials is excellent, such as in aluminum or uranium, the difference between experimental measurement and simulation can be exacerbated in iron or copper, for example. Such deviation seems to be due to limits in the physics models rather than in the discretization methods since similar deviations are observed when these same Lockwood's benchmarks are compared with Monte-Carlo results from TIGER [106] or MCNP6 [110]. GEANT4 models also have been compared to this experimental data [111] and, while they perform better on iron and copper than RADIANT, they are worse in molybdenum and uranium. Such results underline the limit of comparing Monte-Carlo and determinist solvers between themselves, which is widely done in the literature. While such an approach is initially great for developing a cross-section library like the one presented in this section, it can be misleading when attempting to improve the models. However, experimental energy and charge deposition in a semi-infinite medium are rather scarce in the literature, restricted to a few atoms over a limited range of energies. It would be beneficial to systematically have such tabulated experimental data for electron or photon beams for every atom and some compounds (e.g. water) for energies ranging from a few keV to a few GeV. This could significantly impact the development of combined cross-section models for both Monte-Carlo and deterministic solvers.

13. Conclusion

This paper proposes a set of determinist algorithms to solve the coupled radiation transport of positrons, electrons and photons in matter, which are implemented in an open-source code written in Julia programming language. We have presented the Boltzmann Fokker-Planck equation, which is the foundation of the coupled transport of these particles, as well as its multigroup discretization and the resulting energy deposition calculations. From a set of physics models representing the interactions between the three particles, multigroup cross-sections, stopping powers, and momentum transfers have been developed. Subsequently, transport calculations have been conducted on benchmarks selected to attest to the quality of RADIANT algorithms for general-purpose radiation transport of

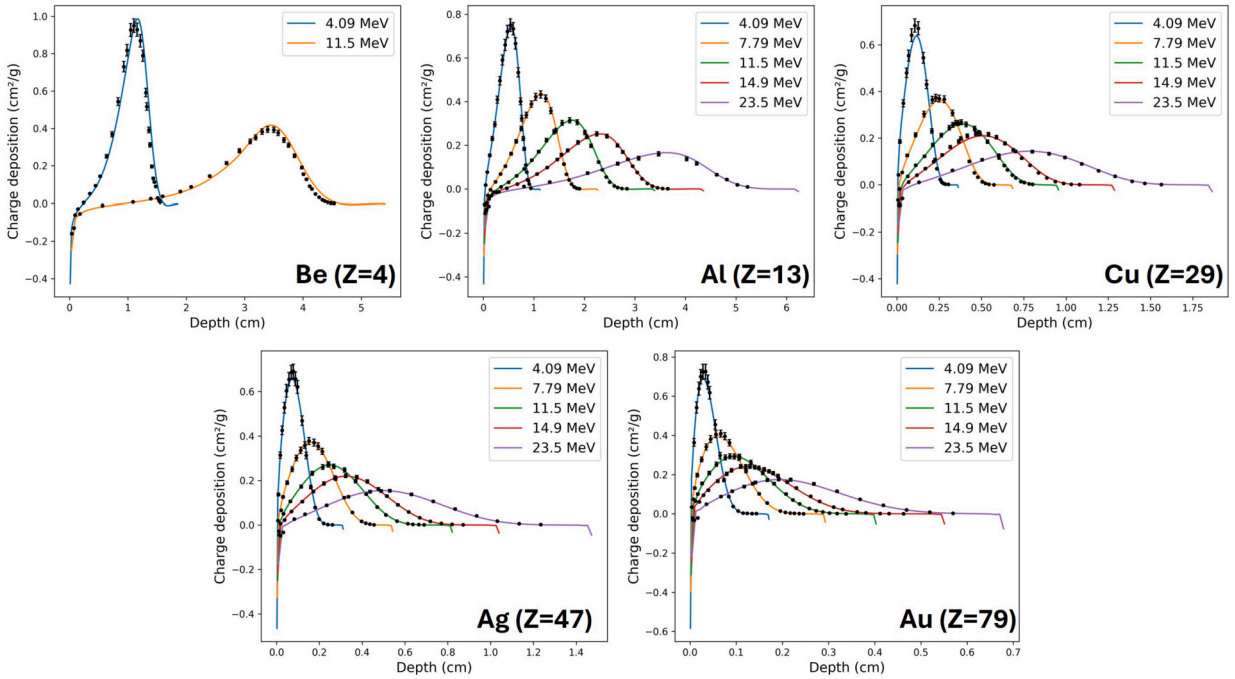

Fig. 6. Charge deposition for normally incident electron beams on beryllium, aluminum, copper, silver and gold. The experimental data comes from Tabata et al. papers [107–109].

photons, electrons, and positrons. The results, consisting of energy spectrum per particle at different depths and energy deposition, are compared to those of the Monte-Carlo reference GEANT4 using PENELOPE models. For energy deposition calculations, agreement of a few percent is observed, but in a few cases. Comparison of energy and charge deposition with experimental measurements is also proposed. The discrepancies between the reference and RADIANT performance are discussed, and a recommendation is provided to improve the underlying models.

CRediT authorship contribution statement

Charles Bienvenue: Writing – review & editing, Writing – original draft, Visualization, Validation, Software, Methodology, Investigation, Data curation, Conceptualization. **Ahmed Naceur:** Writing – review & editing, Investigation, Data curation, Conceptualization. **Alain Hébert:** Writing – review & editing, Validation, Supervision, Funding acquisition, Conceptualization. **Jean-François Carrier:** Writing – review & editing, Validation, Supervision, Funding acquisition, Conceptualization.

Declaration of competing interest

The authors declare the following financial interests/personal relationships which may be considered as potential competing interests: Charles Bienvenue reports financial support was provided by National Sciences and Engineering Research Council (NSERC). If there are other authors, they declare that they have no known competing financial interests or personal relationships that could have appeared to influence the work reported in this paper.

Acknowledgements

This work was supported by the National Sciences and Engineering Research Council (NSERC) through the Discovery Grants program (Application Ids: RGPIN-2021-03899 and RGPIN-2022-03810).

Data availability

Methods and data used in this work should be available in literature and in the code, hosted in a public GitHub repository. If missing, data will be made available on request.

References

[1] J.L. Liscum-Powell, Finite Element Numerical Solution of a Self-Adjoint Transport Equation for Coupled Electron-Photon Problems, The University of New Mexico, 2000.

[2] J.C. Garth, Electron/photon transport and its applications, in: The Monte Carlo Method: Versatility Unbounded in a Dynamic Computing World, Chattanooga, Tennessee, 2005, pp. 17–21.
[3] F. Verhaegen, Monte Carlo modelling of external photon beams in radiotherapy, in: Monte Carlo Techniques in Radiation Therapy, CRC Press, 2021, pp. 43–67.
[4] S. Agostinelli, J. Allison, K.a. Amako, J. Apostolakis, H. Araujo, P. Arce, M. Asai, D. Axen, S. Banerjee, G. Barrand, et al., GEANT4—a simulation toolkit, Nucl. Instrum. Methods Phys. Res., Sect. A, Accel. Spectrom. Detect. Assoc. Equip. 506 (2003) 250–303.
[5] J.-F. Carrier, L. Archambault, L. Beaulieu, R. Roy, Validation of GEANT4, an object-oriented Monte Carlo toolkit, for simulations in medical physics, Med. Phys. 31 (2004) 484–492.
[6] J. Sempau, J. Fernández-Varea, E. Acosta, F. Salvat, Experimental benchmarks of the Monte Carlo code PENELOPE, Nucl. Instrum. Methods Phys. Res., Sect. B, Beam Interact. Mater. Atoms 207 (2003) 107–123.
[7] F. Salvat, J.M. Fernández-Varea, J. Sempau, et al., PENELOPE-2006: a code system for Monte Carlo simulation of electron and photon transport, in: Workshop Proceedings, vol. 4, 2006, p. 7.
[8] I. Kawrakow, D. Rogers, The EGSnrc code system, NRC Report PIRS-701, NRC, Ottawa, 2021.
[9] T. Goorley, M. James, T. Booth, F. Brown, J. Bull, L. Cox, J. Durkee, J. Elson, M. Fensin, R. Forster, et al., Initial MCNP6 release overview, Nucl. Technol. 180 (2012) 298–315.
[10] A.F. Bielajew, D.W. Rogers, PRESTA: the parameter reduced electron-step transport algorithm for electron Monte Carlo transport, Nucl. Instrum. Methods Phys. Res., Sect. B, Beam Interact. Mater. Atoms 18 (1986) 165–181.
[11] E. Boman, Sädehoidon suora ja käänteisongelma Boltzmannin siirtoyhtälön avulla (Radiotherapy forward and inverse problem applying Boltzmann transport equation), Ph.D. thesis, Kuopion yliopisto, 2007.
[12] E. Spezi, G. Lewis, An overview of Monte Carlo treatment planning for radiotherapy, Radiat. Prot. Dosim. 131 (2008) 123–129.
[13] A. Ahnesjö, Collapsed cone convolution of radiant energy for photon dose calculation in heterogeneous media, Med. Phys. 16 (1989) 577–592.
[14] A. Ahnesjö, M. Saxner, A. Trepp, A pencil beam model for photon dose calculation, Med. Phys. 19 (1992) 263–273.
[15] C. Börgers, E.W. Larsen, On the accuracy of the Fokker–Planck and Fermi pencil beam equations for charged particle transport, Med. Phys. 23 (1996) 1749–1759.
[16] L. Brualla, M. Rodriguez, A.M. Lallena, Monte Carlo systems used for treatment planning and dose verification, Strahlenther. Onkol. 193 (2017) 243.
[17] J.L. Bedford, Calculation of absorbed dose in radiotherapy by solution of the linear Boltzmann transport equations, Phys. Med. Biol. 64 (2019) 02TR01.
[18] A. Hébert, Applied Reactor Physics, Presses Inter Polytechnique, 2009.
[19] K. Przybylski, J. Ligou, Numerical analysis of the Boltzmann equation including Fokker-Planck terms, Nucl. Sci. Eng. 81 (1982) 92–109.
[20] J.E. Morel, A hybrid collocation-Galerkin-Sn method for solving the Boltzmann transport equation, Nucl. Sci. Eng. 101 (1989) 72–87.
[21] J.E. Morel, J.S. Warsa, B.C. Franke, A.K. Prinja, Comparison of two Galerkin quadrature methods, Nucl. Sci. Eng. 185 (2017) 325–334.
[22] C.R. Drumm, W.C. Fan, S.D. Pautz, Specializations in the SCEPTRE Code for Charged-Particle Transport, Technical Report, Sandia National Lab. (SNL-NM), Albuquerque, NM (United States), 2018.
[23] A.M. Voloschenko, S.V. Gukov, A.A. Russkov, M.I. Gurevich, D.A. Shkarovsky, V.P. Kryuchkov, O.V. Sumaneev, A.A. Dubinin, The CNCSN-2: One, two- and three-dimensional coupled neutral and charged particle discrete ordinates code system, Technical Report, Keldysh Institute of Applied Mathematics, Moscow, Russia, 2009.
[24] K. Bush, I. Gagne, S. Zavgorodni, W. Ansbacher, W. Beckham, Dosimetric validation of Acuros® XB with Monte Carlo methods for photon dose calculations, Med. Phys. 38 (2011) 2208–2221.
[25] K.A. Gifford, J.L. Horton, T.A. Wareing, G. Failla, F. Mourtada, Comparison of a finite-element multigroup discrete-ordinates code with Monte Carlo for radiotherapy calculations, Phys. Med. Biol. 51 (2006) 2253.
[26] O.N. Vassiliev, T.A. Wareing, J. McGhee, G. Failla, M.R. Salehpour, F. Mourtada, Validation of a new grid-based Boltzmann equation solver for dose calculation in radiotherapy with photon beams, Phys. Med. Biol. 55 (2010) 581.
[27] A. Hébert, DRAGON5 and DONJON5, the contribution of École Polytechnique de Montréal to the SALOME platform, Ann. Nucl. Energy 87 (2016) 12–20.
[28] A. Naceur, A. Hébert, P. Romano, B. Forget, C. Chilian, J.-F. Carrier, Feasibility of a multigroup Boltzmann–Fokker–Planck solution for electron beam dose calculations, Sci. Rep. 13 (2023) 1310.
[29] L. Lorence Jr, J. Morel, G. Valdez, Physics guide to CEPXS: a multigroup coupled electron-photon cross-section generating code, Technical Report, Sandia National Lab. (SNL-NM), Albuquerque, NM (United States), 1989.
[30] H. Hensel, R. Iza-Teran, N. Siedow, Deterministic model for dose calculation in photon radiotherapy, Phys. Med. Biol. 51 (2006) 675.
[31] E. Olbrant, M. Frank, Generalized Fokker–Planck theory for electron and photon transport in biological tissues: application to radiotherapy, Comput. Math. Methods Med. 11 (2010) 313–339.
[32] R.E. MacFarlane, D.W. Muir, The NJOY nuclear data processing system version 91, Technical Report, Los Alamos National Lab., NM, United States, 1994.
[33] A. Trkov, D.A. Brown, ENDF-6 Formats Manual: Data formats and procedures for the evaluated nuclear data files, Technical Report, Brookhaven National Lab. (BNL), Upton, NY (United States), 2018.
[34] A. Naceur, C. Bienvenue, P. Romano, C. Chilian, J.-F. Carrier, Extending deterministic transport capabilities for very-high and ultra-high energy electron beams, Sci. Rep. 14 (2024) 2796.
[35] A. Hébert, A. Naceur, Implementation of the ELECTR Module in NJOY, EPJ Web of Conferences, vol. 284, EDP Sciences, 2023, p. 11001.
[36] X. Li, Y. Li, R. Shao, N. Xu, L. Cao, T. Zu, Y. Liang, J. Qin, W. Shen, Multigroup cross-section data processing for deterministic electron-transport calculation, in: International Conference on Physics of Reactors (PHYSOR 2024), 2024.
[37] A. Naceur, P. Romano, C. Chilian, J.-F. Carrier, Granularity Level Requirements for Multigroup Evaluated Electron Data Library Use in Boltzmann-Fokker-Planck Codes: a Bremsstrahlung Case Study, 2024.
[38] A.M. Voloschenko, CEPXS-BFP: Version of Multigroup Coupled Electron-Photon Cross-Section Generating Code CEPXS, Adapted for Solving the Charged Particle Transport in the Boltzmann Fokker-Planck Formulation with the Use of Discrete Ordinate Method. User's Guide, Report of Keldysh Inst. of Appl. Math., Russian Ac. of Sci., No. 7-36-2004, Technical Report 2004.
[39] J. Bezanson, A. Edelman, S. Karpinski, V.B. Shah, Julia: a fresh approach to numerical computing, SIAM Rev. 59 (2017) 65–98.
[40] A. Voloschenko, S. Gukov, A. Shwetsov, ARVES-2.5: Preprocessor for the Working Macroscopic Cross-Section FMAC-M Format for Transport Calculations User's Guide, Technical Report, Keldysh Institute of Applied Mathematics, Moscow, Russia, 2004.
[41] C. Bienvenue, Radiant (v1.0.0), https://github.com/CBienvenue/Radiant.jl, 2024.
[42] E.E. Lewis, W.F. Miller, Computational Methods of Neutron Transport, John Wiley and Sons, Inc., New York, NY, 1984.
[43] G. Pomraning, The Fokker-Planck operator as an asymptotic limit, Math. Models Methods Appl. Sci. 2 (1992) 21–36.
[44] C. Bienvenue, A. Hébert, High-order diamond differencing schemes for the Boltzmann Fokker–Planck equation in 1D and 2D Cartesian geometries, Ann. Nucl. Energy 171 (2022) 109032.
[45] J. Morel, L.J. Lorence Jr, R.P. Kensek, J.A. Halbleib, D. Sloan, A hybrid multigroup/continuous-energy Monte Carlo method for solving the Boltzmann-Fokker-Planck equation, Nucl. Sci. Eng. 124 (1996) 369–389.
[46] P. Andreo, D.T. Burns, A.E. Nahum, J. Seuntjens, F.H. Attix, Fundamentals of Ionizing Radiation Dosimetry, John Wiley & Sons, 2017.
[47] F. Salvat, J.M. Fernández-Varea, Overview of physical interaction models for photon and electron transport used in Monte Carlo codes, Metrologia 46 (2009) S112.
[48] S. Perkins, Tables and Graphs of Atomic Subshell and Relaxation Data Derived from the LLNL Evaluated Atomic Data Library (EADL), Z = 1-100, Lawrence Livermore National Laboratory, 1991.

[49] C. Møller, Zur theorie des durchgangs schneller elektronen durch materie, Ann. Phys. 406 (1932) 531–585.
[50] S. Perkins, D. Cullen, The Livermore electron impact ionization data base, Technical Report, Lawrence Livermore National Lab. (LLNL), Livermore, CA (United States), 1989.
[51] H. Bhabha, The scattering of positrons by electrons with exchange on Dirac's theory of the positron, Proc. R. Soc. Lond. Ser. A, Math. Phys. Sci. 154 (1936) 195–206.
[52] F. Salvat, P. Andreo, SBETHE: stopping powers of materials for Swift charged particles from the corrected Bethe formula, Comput. Phys. Commun. 287 (2023) 108697.
[53] S.M. Seltzer, M.J. Berger, Evaluation of the collision stopping power of elements and compounds for electrons and positrons, Int. J. Appl. Radiat. Isot. 33 (1982) 1189–1218.
[54] S. Seltzer, J. Fernandez-Varea, P. Andreo, P. Bergstrom, D. Burns, I. Krajcar Bronić, C. Ross, F. Salvat, Key data for ionizing-radiation dosimetry: measurement standards and applications, ICRU Report 90, 2016.
[55] F. Salvat, Bethe stopping-power formula and its corrections, Phys. Rev. A 106 (2022) 032809.
[56] F. Rohrlich, B. Carlson, Positron-electron differences in energy loss and multiple scattering, Phys. Rev. 93 (1954) 38.
[57] U. Fano, Atomic theory of electromagnetic interactions in dense materials, Phys. Rev. 103 (1956) 1202.
[58] M. Inokuti, D.Y. Smith, Fermi density effect on the stopping power of metallic aluminum, Phys. Rev. E 25 (1982) 61.
[59] R.M. Sternheimer, The density effect for the ionization loss in various materials, Phys. Rev. 88 (1952) 851.
[60] S.M. Seltzer, An overview of ETRAN Monte Carlo methods, in: Monte Carlo Transport of Electrons and Photons, 1988, pp. 153–181.
[61] G. Moliere, Theorie der streuung schneller geladener teilchen i. Einzelstreuung am abgeschirmten Coulomb-Feld, Z. Naturforsch. A 2 (1947) 133–145.
[62] T. Lijian, H. Qing, L. Zhengming, Analytic fitting to the Mott cross section of electrons, Radiat. Phys. Chem. 45 (1995) 235–245.
[63] M. Boschini, C. Consolandi, M. Gervasi, S. Giani, D. Grandi, V. Ivanchenko, P. Nieminem, S. Pensotti, P. Rancoita, M. Tacconi, An expression for the Mott cross section of electrons and positrons on nuclei with Z up to 118, Radiat. Phys. Chem. 90 (2013) 39–66.
[64] U. Fano, Inelastic collisions and the Moliere theory of multiple scattering, Phys. Rev. 93 (1954) 117.
[65] X.A. Li, D. Rogers, Electron mass scattering powers: Monte Carlo and analytical calculations, Med. Phys. 22 (1995) 531–541.
[66] I. Kawrakow, Improved modeling of multiple scattering in the voxel Monte Carlo model, Med. Phys. 24 (1997) 505–517.
[67] W. Koepf, Hypergeometric Summation, Vieweg, Braunschweig/Wiesbaden 5, 1998.
[68] I.S. Gradshteyn, I.M. Ryzhik, Table of Integrals, Series, and Products, Academic Press, 2014.
[69] Á. Elbert, A. Laforgia, An inequality for Legendre polynomials, J. Math. Phys. 35 (1994) 1348–1360.
[70] M. Landesman, J. Morel, Angular Fokker-Planck decomposition and representation techniques, Nucl. Sci. Eng. 103 (1989) 1–11.
[71] J. Morel, Fokker-Planck calculations using standard discrete ordinates transport codes, Nucl. Sci. Eng. 79 (1981) 340–356.
[72] Y. Azmy, E. Sartori, E.W. Larsen, J.E. Morel, Advances in discrete-ordinates methodology, in: Nuclear Computational Science: a Century in Review, 2010, pp. 1–84.
[73] J.E. Morel, An improved Fokker-Planck angular differencing scheme, Nucl. Sci. Eng. 89 (1985) 131–136.
[74] J.E. Morel, A. Prinja, J.M. McGhee, T.A. Wareing, B.C. Franke, A discretization scheme for the three-dimensional angular Fokker-Planck operator, Nucl. Sci. Eng. 156 (2007) 154–163.
[75] J. Morel, On the validity of the extended transport cross-section correction for low-energy electron transport, Nucl. Sci. Eng. 71 (1979) 64–71.
[76] C.R. Drumm, W.C. Fan, L. Lorence, J. Liscum-Powell, An analysis of the extended-transport correction with application to electron beam transport, Nucl. Sci. Eng. 155 (2007) 355–366.
[77] S.M. Seltzer, M.J. Berger, Bremsstrahlung energy spectra from electrons with kinetic energy 1 keV–10 GeV incident on screened nuclei and orbital electrons of neutral atoms with Z= 1–100, At. Data Nucl. Data Tables 35 (1986) 345–418.
[78] F.N. Fritsch, R.E. Carlson, Monotone piecewise cubic interpolation, SIAM J. Numer. Anal. 17 (1980) 238–246.
[79] L. Kim, R. Pratt, S. Seltzer, M. Berger, Ratio of positron to electron bremsstrahlung energy loss: an approximate scaling law, Phys. Rev. A 33 (1986) 3002.
[80] E. Acosta, X. Llovet, F. Salvat, Monte Carlo simulation of bremsstrahlung emission by electrons, Appl. Phys. Lett. 80 (2002) 3228–3230.
[81] F. Salvat, J. Fernández-Varea, J. Sempau, X. Llovet, Monte Carlo simulation of bremsstrahlung emission by electrons, Radiat. Phys. Chem. 75 (2006) 1201–1219.
[82] A. Poškus, Shape functions and singly differential cross sections of bremsstrahlung at electron energies from 10 eV to 3 MeV for Z= 1–100, At. Data Nucl. Data Tables 129 (2019) 101277.
[83] L. Kissel, C. Quarles, R. Pratt, Shape functions for atomic-field bremsstrahlung from electrons of kinetic energy 1–500 keV on selected neutral atoms $1 \leq Z \leq 92$, At. Data Nucl. Data Tables 28 (1983) 381–460.
[84] W. Heitler, The Quantum Theory of Radiation, Courier Corporation, 1984.
[85] GEANT Collaboration, Physics reference manual, Technical Report, CERN, Switzerland, 2016.
[86] J.H. Hubbell, W.J. Veigele, E. Briggs, R. Brown, D. Cromer, d.R. Howerton, Atomic form factors, incoherent scattering functions, and photon scattering cross sections, J. Phys. Chem. Ref. Data 4 (1975) 471–538.
[87] O. Iwamoto, N. Iwamoto, S. Kunieda, F. Minato, S. Nakayama, Y. Abe, K. Tsubakihara, S. Okumura, C. Ishizuka, T. Yoshida, et al., Japanese evaluated nuclear data library version 5: JENDL-5, J. Nucl. Sci. Technol. 60 (2023) 1–60.
[88] D.E. Cullen, M. Chen, J. Hubbell, S. Perkins, E. Plechaty, J. Rathkopf, J. Scofield, Tables and graphs of photon-interaction cross sections from 10 eV to 100 GeV derived from the LLNL evaluated photon data library (EPDL), Technical Report, Lawrence Livermore National Lab., CA (USA), 1989.
[89] D. Brusa, G. Stutz, J. Riveros, J. Fernández-Varea, F. Salvat, Fast sampling algorithm for the simulation of photon Compton scattering, Nucl. Instrum. Methods Phys. Res., Sect. A, Accel. Spectrom. Detect. Assoc. Equip. 379 (1996) 167–175.
[90] F. Sauter, Über den atomaren photoeffekt in der k-schale nach der relativistischen wellenmechanik diracs, Ann. Phys. 403 (1931) 454–488.
[91] J. Baró, M. Roteta, J. Fernández-Varea, F. Salvat, Analytical cross sections for Monte Carlo simulation of photon transport, Radiat. Phys. Chem. 44 (1994) 531–552.
[92] Y.-S. Tsai, Pair production and bremsstrahlung of charged leptons, Rev. Mod. Phys. 46 (1974) 815.
[93] H. Davies, H. Bethe, L. Maximon, Theory of bremsstrahlung and pair production. II. Integral cross section for pair production, Phys. Rev. 93 (1954) 788.
[94] M.S. Lazo, J. Morel, A linear discontinuous Galerkin approximation for the continuous slowing down operator, Nucl. Sci. Eng. 92 (1986) 98–109.
[95] J. Honrubia, J. Aragonés, Finite element method for charged-particle calculations, Nucl. Sci. Eng. 93 (1986) 386–402.
[96] C. Bienvenue, A. Naceur, J.-F. Carrier, A. Hébert, Adaptive gradient-driven coupled linear schemes and their usefulness for charged particle transport, in: International Conference on Mathematics and Computational Methods Applied to Nuclear Science and Engineering (M&C 2023), 2023.
[97] R. Sanchez, J. Ragusa, On the construction of Galerkin angular quadratures, Nucl. Sci. Eng. 169 (2011) 133–154.
[98] P. Andreo, A. Brahme, Restricted energy-loss straggling and multiple scattering of electrons in mixed Monte Carlo procedures, Radiat. Res. 100 (1984) 16–29.
[99] J.S. Warsa, A.K. Prinja, p-Adaptive numerical methods for particle transport, Transp. Theory Stat. Phys. 28 (1999) 229–270.
[100] M. Asai, M.A. Cortés-Giraldo, V. Giménez-Alventosa, V. Giménez Gómez, F. Salvat, The penelope physics models and transport mechanics. Implementation into geant4, Front. Phys. 9 (2021) 738735.
[101] J.H. Renken, Legendre polynomial expansion for the Klein-Nishina formula, J. Appl. Phys. 38 (1967) 4925–4927.
[102] J. Hubbell, S.M. Seltzer, Cross section data for electron–positron pair production by photons: a status report, Nucl. Instrum. Methods Phys. Res., Sect. B, Beam Interact. Mater. Atoms 213 (2004) 1–9.

[103] V. Ivanchenko, O. Kadri, M. Maire, L. Urban, Geant4 Models for Simulation of Multiple Scattering, Journal of Physics: Conference Series, vol. 219, IOP Publishing, 2010, p. 032045.
[104] D. Bote, F. Salvat, Calculations of inner-shell ionization by electron impact with the distorted-wave and plane-wave Born approximations, Phys. Rev. A 77 (2008) 042701.
[105] D. Bote, F. Salvat, A. Jablonski, C.J. Powell, Cross sections for ionization of K, L and M shells of atoms by impact of electrons and positrons with energies up to 1 GeV: analytical formulas, At. Data Nucl. Data Tables 95 (2009) 871–909.
[106] G.J. Lockwood, L.E. Ruggles, G.H. Miller, J. Halbleib, Calorimetric measurement of electron energy deposition in extended media. Theory vs experiment, Technical Report, Sandia National Lab. (SNL-NM), Albuquerque, NM (United States), 1980.
[107] T. Tabata, Backscattering of electrons from 3.2 to 14 mev, Phys. Rev. 162 (1967) 336.
[108] T. Tabata, R. Ito, S. Okabe, Y. Fujita, Charge distribution produced by 4-to 24-mev electrons in elemental materials, Phys. Rev. B 3 (1971) 572.
[109] T. Tabata, R. Ito, S. Okabe, An empirical equation for the backscattering coefficient of electrons, Nucl. Instrum. Methods 94 (1971) 509–513.
[110] C.J. Josey, A.R. Clark, J.A. Kulesza, E.J. Pearson, M.E. Rising, Mcnp® code version 6.3. 0 verification & validation testing, Tech. Rep. LA-UR-22-32951, Los Alamos National Laboratory, Los Alamos, New Mexico, USA, 2022, p. 20.
[111] A. Lechner, M.G. Pia, M. Sudhakar, Validation of geant4 low energy electromagnetic processes against precision measurements of electron energy deposition, IEEE Trans. Nucl. Sci. 56 (2009) 398–416.